Role of channels in the O_2 permeability of murine red blood cells
II. Morphological and proteomic studies

Fraser J. Moss[1]
Pan Zhao[1]
Ahlam I. Salameh[1]
Sara Taki[1]
Amanda B. Wass[1]
James W. Jacobberger[3]
Dale E. Huffman[1]
Howard J. Meyerson[2]
Rossana Occhipinti[1]
Walter F. Boron[1]

[1]Department of Physiology & Biophysics, and [2]Department of Pathology
Case Western Reserve University School of Medicine, and [3]Case Comprehensive Cancer Center,
Cleveland, OH 44106, United States

Section: *Journal of Physiology*, Cell physiology

Running title: RBC O_2 permeability: Morphology

Keywords: O_2 permeability, Red Blood Cells, Red Blood Cell Morphology, Proteomics

Correspondence and proofs:
Walter F Boron, MD, PhD
Department of Physiology and Biophysics
Case Western Reserve University
School of Medicine
10900 Euclid Avenue
Cleveland, OH 44106-4970
Phone: (216) 368 3400
Fax: (216) 368 5586
E-mail Walter.Boron@case.edu

Key Points

- O_2-offloading from red blood cells (RBCs) depends not only on membrane O_2 permeability and dissociation of oxyhemoglobin (HbO_2), but also on RBC size and shape. In this second of three papers, we use blood smears, still/video images of living RBCs, and imaging flow cytometry (IFC) to examine morphometry of RBCs from paper #1.
- We find that mouse RBCs of all genotypes—wild-type (WT), aquaporin-1 knockout (AQP1-KO), Rhesus blood group-associated A-glycoprotein knockout (RhAG-KO), and double knockout (dKO)—are dominantly biconcave discs, with ~2% poikilocytosis (shape change, SC). Drug pre-treatment increases %SC.
- Using label-free liquid chromatography/tandem mass spectrometry (LC/MS/MS) to assess apparent abundance of RBC-ghost proteins , we find no significant differences among genotypes for any of the ~100 most abundant proteins except, as appropriate, AQP1, RhAG, or Rhesus blood group D antigen (RhD).
- Thus, the substantial effects observed in paper #1 cannot be attributed to differences in morphometry or protein content.

Abstract

In this second of three papers, we examine the morphometry of red blood cells (RBCs) from our laboratory mouse strain (C57BL/6_{Case}) and RBC-membrane proteomics. In paper #1, using stopped-flow absorbance-spectroscopy to ascertain the rate constant for oxyhemoglobin (HbO_2) deoxygenation (k_{HbO2}), we find substantial reductions in k_{HbO2} with (1) membrane-protein inhibitors p-chloromercuribenzenesulfonate (pCMBS) or 4,4'-diisothiocyanatostilbene-2,2'-disulfonate (DIDS); (2) knockouts of aquaporin-1 (AQP1-KO), or Rhesus blood-group–associated A-glycoprotein (RhAG-KO), or double knockouts (dKO); or (3) inhibitor+dKO. In paper #3, reaction-diffusion mathematical modeling/simulations reveal that k_{HbO2} could have fallen secondary to: (a) slowed O_2/HbO_2/Hb diffusion through RBC cytosol, due to increased diffusion distances and (b) decreased membrane O_2 permeability, due to changes in membrane-protein composition. Here in paper #2, blood smears as well as still/video images and imaging flow cytometry (IFC) of living RBCs show that >98% of control (not drug-treated) cells are biconcave disks (BCDs) across all genotypes. Pretreatment with pCMBS raises non-BCD abundance to ~8.7% for WT and ~5.7%% for dKO; for DIDS pretreatment, the figures are ~41% and ~21%, respectively. Modeling (paper #3) accommodates for these shape changes. Light-scattering flow cytometry shows no significant difference in RBC size or shape among genotypes. IFC reveals minor differences among genotypes in RBC major diameter ($Ø_{Major}$), which (along with mean corpuscular volume, paper #1) yields RBC thickness for paper-#3 simulations. Label-free liquid chromatography/tandem mass spectrometry (LC/MS/MS) proteomic analyses of RBC plasma-membrane ghosts rule out protein-abundance contributions to k_{HbO2} from major membrane proteins other than those targeted in KO studies.

Introduction

The uptake of O_2 by red blood cells (RBCs) in the pulmonary capillaries, the carriage of O_2 to the systemic tissues, and the offloading of O_2 from RBCs in the systemic capillaries to support oxidative metabolism is central to the life of every mammal. Some investigators, influenced by an implicit assumptions underlying the mathematical formulation of Krogh's cylinder (Krogh, 1919; Kreuzer, 1982), have believed that membranes, including RBC membranes, offer no resistance to O_2 diffusion. Others, influenced by Overton (for reviews, see Missner & Pohl, 2009; Boron, 2010), contend that while membranes offer resistance to O_2 diffusion, the rate is solely contingent upon O_2 solubility in membrane lipids (Forstner & Gnaiger, 1983).

The present paper is the second in a series of three interdependent papers[1] that investigate the extent to which murine aquaporin-1 (AQP1), the Rh complex (mouse Rh_{Cx} = Rhesus blood group-associated A-glycoprotein, RhAG + Rhesus blood group D antigen, RhD), and potentially other RBC membrane proteins contribute to the O_2 permeability of the murine RBC membrane (P_{M,O_2}).

In the first paper (paper #1; Zhao *et al.*, 2025), we expose murine RBCs to an O_2 scavenger (creating an O_2-free environment) in a stopped-flow (SF) absorbance-spectroscopy apparatus to determine the rate constant for Hb deoxygenation (k_{HbO_2}). We find that k_{HbO_2} falls markedly if we pretreat RBCs with p-chloromercuribenzenesulfonate (pCMBS) or 4,4'-diisothiocyanatostilbene-2,2'-disulfonate (DIDS)—known inhibitors of CO_2-conducting channels—or if we obtain the RBCs from our laboratory strain of mice (C57BL/6_{Case}) genetically deficient in *Aqp1* (i.e., *Aqp1*–

[1] As a shorthand, we will refer to the three papers as "paper #1", "paper #2", and "paper #3".

/– genotype), *Rhag* (*Rhag*–/– genotype), or both (*Aqp1*–/–*Rhag*–/– genotype). Of course, k_{HbO_2} depends not only on P_{M,O_2} but also the diffusion of O_2, oxyhemoglobin (HbO_2), and hemoglobin (Hb) through the cytosol of the RBC, as well as the rate of O_2 dissociation from HbO_2 per se. Thus, in paper #1, we measure mean corpuscular volume (MCV), mean corpuscular hemoglobin (MCH), and mean corpuscular hemoglobin concentration (MCHC), other automated hematological parameters, and the rate constant ($k_{HbO2 \rightarrow Hb}$) of the reaction $HbO_2 \rightarrow Hb + O_2$ in fully hemolyzed RBCs (i.e., in the absence of intact membranes). Paper #1 also provides a brief summary of the essential contributions of paper #2 (the present paper) and paper #3.

In this second (the present) paper, we assess RBC morphology at a microscopic scale—including blood smears, still and video images of living RBCs, and imaging flow cytometry (IFC). We ask whether the cells are mature RBCs and shaped as biconcave discs (BCDs) and, if they are not, determine the abundance and other characteristics of these other cells (i.e., poikilocytes), collectively termed non-BCDs (nBCDs). The IFC approach allows us to determine RBC major diameter ($Ø_{Major}$), which—together with the above MCV—allow us to compute RBC thickness—an important input for the mathematical simulations (see next paragraph). The present paper also includes a proteomic analysis of RBC ghosts to determine whether the knockout (KO) of *Aqp1* and/or *Rhag* produces unexpected effects in the protein composition of the RBC membranes. We find that the RBC membranes of mice genetically deficient in *Aqp1* and/or *Rhag* lack only the intended proteins among the 100 proteins with the greatest inferred abundance. Here in paper #2, we make frequent reference to relevant elements in paper #1 and paper #3.

In paper #3 (Occhipinti *et al.*, 2025), we report a novel reaction-diffusion model of O_2 unloading from a RBC and the resulting mathematical simulations of the experiments from the paper #1. Importantly, these simulations draw from the MCV, MCH, and MCHC data from paper #1, as well as the BCD, nBCD data and $Ø_{Major}$ data from this second (i.e., the present) paper. The

simulations agree rather well with the physiological data, allowing us to extract P_{M,O_2} values from the simulated k_{HbO2} data.

Together, the three papers show that RBC membranes of wild-type (WT) mice offer considerable resistance to O_2 diffusion, thereby ruling out the implicit assumption of Krogh. Nevertheless, the resistance would be 10-fold higher yet if it were not for the P_{M,O_2} contributions of AQP1 (~22%), Rh_{Cx} (~33%), and at least one unidentified non-AQP1/non-Rh_{Cx} pathway that is blocked by pCMBS. These results rule out the Overton hypothesis, at least for RBCs. Thus, this work changes the way we think of RBC O_2 handling, and raises the possibility of modulating P_{M,O_2} by manipulating membrane proteins.

Methods

Ethical approval and animal procedures

All animal procedures are reviewed and approved by the Institutional Animal Care and Use Committee (IACUC) at Case Western Reserve University (CWRU).

Mice

The mice and the methodologies concerning the mice are the same as in paper #1 (Zhao *et al.*, 2025)[2].

Genotyping

The genotyping methodologies are the same as in paper #1[3].

Physiological solutions

The physiological solutions are a subset of those summarized in paper #1[4], and replicated here as Table 1. We make pH measurements at room temperature (RT) for the present paper (note that in SF experiments for paper #1, we titrated solutions at 10°C) using a portable pH meter (model A121 Orion Star, Thermo Fischer Scientific (TFS), Waltham, MA) fitted with a pH

---

[2] See paper #1>Methods>Mice. As a further shorthand, and to aid the reader to locating the precise target, the ">" symbol separates heading levels. It is understood that the reference is to a location in the present paper unless "See" is followed by "paper #1" or "paper #3".

[3] See paper #1>Methods>Genotyping

[4] See paper #1>Table 2

electrode (Ross Sure-Flow combination pH Electrode, TFS). Beakers containing pH calibration buffers (pH at 6, 8 and 10; TFS), physiological solutions to be titrated, and the pH electrode in its storage solution (Beckman Coulter, Inc. Brea, CA) are all equilibrated at RT. We adjust pH with NaOH (5 M) or HCl (5 M). Osmolality is measured using a vapor pressure osmometer (Vapro 5520; Wescor, Inc., Logan, UT) and, as necessary, adjusted upward by addition of NaCl.

Inhibitors

The inhibitors and their sourcing are the same as paper #1[5]. We freshly prepare stock solutions of 2 mM pCMBS and 2 mM DIDS by dissolving the agents directly into our "Oxygenated solution" (see Table 1), taking care to shield the solutions from light.

Preparation of RBCs

Paper #1[6] provides an overview of our approaches for collecting and preparing RBCs for various assays. Here we allude to general methodology for the sake of context, but focus on the methods particularly relevant to this second (the present) paper.

Collection of blood from mice. We collect fresh blood from WT or KO mice for seven assays: (1) SF, (2) still microphotography, (3) microvideography, (4) flow cytometry, (5) automated hematology, (6) blood smears, and (7) proteomics/mass spectrometry. For the work in the present paper, we collect blood (~250 μl) exclusively using the submandibular-bleed method (Golde *et al.*, 2005) with a 3-, 4-, or 5-mm point-length sterile animal lancet (MEDIpoint, Inc.,

[5] See paper #1>Methods>Inhibitors

[6] See paper #1>Methods>Preparation of RBCs

Mineola, NY). We return to the same mouse no sooner than 72 h from a previous blood sample, using the contralateral side.

Processing of RBCs for assays 1–4. For the first four assays in the above list—SF (in paper #1[7]) as well as still microphotography, microvideography, and flow cytometry (the others in the present paper)—we collect blood into 1.7-ml microcentrifuge tubes that are previously rinsed with 0.1% sodium heparin (H4784, Sigma-Aldrich, St. Louis, MO), and then centrifuged in a Microfuge 16 Microcentrifuge (Beckman Coulter, Inc.) at 600 × g for 10 min. We aspirate and discard the resulting supernatant and buffy coat. To remove residual extracellular Hb, we resuspend the pelleted RBCs in our oxygenated solution (Table 1) to a hematocrit (Hct) of 5% to 10%, centrifuged at 600 × g for 5 min. After 4 such washes, we resuspend RBCs in oxygenated solution to a final Hct of 25% to 30%, and maintain on ice (for up to ~6 h) for experiments. At this point, the RBCs are directed to studies of SF (see paper #1)[8], still microphotography and microvideography (see below)[9], or flow-cytometry (see below)[10].

---

[7] See paper #1>Methods>Preparation of RBCs>First four assays

[8] See paper #1>Methods>Preparation of RBCs>Processing of RBCs for stopped-flow studies

[9] See Methods>Still microphotography and microvideography of living RBCs

[10] See Methods>Flow cytometry (workflow #6 & #11)

Automated hematology. For automated hematological studies (see paper #1[11]), we collect whole blood into 20-µl plastic Boule MPA Micro pipettes (EDTA-K2, Boule Medical AB, Stockholm, Sweden).

Blood smears. For blood-smear studies (see below[12]), we collect whole blood into 2 ml K2E K2EDTA VACUETTE® tubes (Grelner Bio-One North America Inc, Monroe, NC).

Proteomic analysis. For proteomic analysis/mass spectrometry (see below[13]) we collect whole blood into 1.7-ml heparinized microcentrifuge tubes.

Blood smears

Preparation of RBCs. We collect fresh blood from 3 mice of each genotype (see above[14]) into 2-ml K2E K2EDTA VACUETTE® tubes (Monroe, NC 28110, USA). Blood smears are prepared using microscope slides (Fisher scientific, Pittsburgh, USA), and stained using Wright's stain on a Sysmex SP-10 autostainer (Kobe, Japan). Air-dried smears are placed in staining cassettes, and staining performed per manufacturer's specifications. Blood smears images (1000× magnification) are taken on an Olympus BH-2 microscope (Tokyo, Japan) with a DP73 digital camera attachment (Olympus), visualized with cellSens software (Olympus), and reviewed by a board-certified hematopathologist (H.J.M.).

---

[11] See paper #1>Methods>Automated hematological analyses (workflow #7–9)

[12] See Methods>Blood smears

[13] See Methods>Proteomic analysis

[14] See Methods>Preparation of RBCs>Collection of blood

Use of inhibitors in blood-smear studies. After 2 washes, we resuspend packed RBCs into our oxygenated solution (see Table 1; [Hb] = 5 μM, Hct ≅ 0.3%) without drugs or with either pCMBS (1 mM for 15 min) or DIDS (200 μM for 1 hour). After centrifuging RBCs at 600 × g for 5 min, we aspirate and discard the resulting supernatant to remove inhibitors. RBCs are then resuspended in our oxygenated solution to make blood smears, following our standard procedure, outlined in the previous paragraph. We repeat this on three different days, for a total of 3 mice of each genotype.

Still microphotography and microvideography of living RBCs

We perform experiments (still or video imaging) on fresh blood, collected and processed as described above[15], one sample per mouse for each of four genotypes, all on the same day. We repeat this on three different days, for a total of 3 mice of each genotype, for both still and video studies (i.e., a total of 3+3 mice/genotype). After 4 washes and dilution of RBCs to an Hct of 25% to 30%, we suspend the cells in our oxygenated solution (see Table 1) to a final Hct of 0.5% to 1%, and store on ice for 30 – 120 min before imaging.

In preparation for the experiment, we acid-wash coverslips by immersing them in 2 M HCl for 30 min, performing 3 × 5 min washes with DNAase-/RNAase-free water, and finally immersed them in 100% ethanol for 30 min before final air drying. A droplet containing suspended RBCs from one mouse (see previous paragraph) is placed on one of these acid-washed glass coverslips that served as the bottom of a recording chamber. The chamber is then mounted on Olympus IX-81 inverted microscope equipped for differential interference contrast (DIC) studies, using either of two oil immersion objectives (60× objective, NA 1.42 for still micrographs or 40× objective,

[15] See Methods>Preparation of RBCs>Collection of blood from mice.>Processing of RBCs for assays 1–4

NA 1.35 for microvideomicroscopy) with a 1.5× magnification selector. The light is detected with an intensified EM-CCD camera (C9100-13, Hamamatsu Corporation, Bridgewater, NJ) with 512 × 512 pixels, and data acquired using SlideBook 5.0 software (Intelligent Imaging Innovation, Denver, CO) for the Hamamatsu camera. We record still micrographs or microvideos (1 frame per 5 sec) of the RBC droplet as RBCs fall freely through the plane of focus, toward the coverslip surface.

Use of inhibitors in still photomicrography. After 4 washes, as noted in the previous paragraph, we resuspend packed RBCs in our oxygenated solution (see Table 1) without drugs or with either pCMBS (1 mM for 15 min) or DIDS (200 μM for 1 hour) to a final Hct of 1% to 2%, and direct the RBCs to still-photomicrography studies.

Flow cytometry (workflow #6 & #11)

All flow cytometry experiments are performed at the Case Comprehensive Cancer Center Cytometry and Microscopy Share Resource at CWRU (CMSR).

Sample preparation. On a single day, we collect fresh blood (see above[16]) from 2 mice of each genotype. We repeat experiments on another day, for a total of 4 mice per genotype. To permit gating of viable RBC precursors, we dilute 100-μl samples of cells to a 1% Hct in our oxygenated solution (see Table 1) containing 1 μM Calcein Violet (CV; viability marker; excitation/emission 405⁄450 nm; TFS, C3099), 0.1 μg/ml Thiazol Orange (TO; to stain RNA; 490⁄530 nm; Sigma-Aldrich 390062), and 5 μM DRAQ-5 (to stain DNA; 647⁄683 nm; TFS, 62252), and then incubate for 20 min at RT in the dark. We then wash the dye-loaded RBC samples ×3 in 1 ml of our oxygenated solution, centrifuging at 600×g for 5 min between washes, and

[16] See Methods>Preparation of RBCs>Collection of blood

maintained stained cells on ice for up to ~2 h on ice for experiments. The Hct was either 0.06% Hct (~2 million cells/ml) for light scattering on the LSRII or 1 % Hct for imaging on the ImageStream instrument.

Light-scattering flow cytometry. The first step is to generate a histogram—over a single sample of cells—that describes the relative number of cells (y-axis) vs. amount of scattered light (x-axis) (Loken *et al.*, 1977). Forward scatter—measured by photodiodes positioned in line with the incident light source—is proportional to cell size. Forward-scatter intensity area (FSC-A) is the cumulative integration of the forward-scatter signal for the full period a cell traverses the laser path, specifically the total area underneath the corresponding histogram. The FSC-A parameter provides overall size and shape information for the cell, utilized alongside forward scatter pulse height (FSC-H), which quantifies the amplitude of the detected light scatter signal as cells traverse the laser beam, indicating cell size, and forward-scatter intensity width (FSC-W), which measures the duration of the cell's passage through the laser beam, indicating size variability and aiding in the differentiation between individual cells and aggregates.

FSC-A, FSC-H, FSC-W, as well as the fluorescence of CV, TO, and DRAQ-5, are measured with an LSRII flow cytometer (BD Biosciences; San Jose, CA). To exclude aggregates and debris we set an FSC-A/FSC-H gate (R1, Figure 5*A*). To focus on the erythrocytic cells (RBCs and reticulocytes), we set gates on the dim or negative cells in TO vs CV (R2, Figure 5*B*) and TO vs DRAQ-5 (R4, Figure 5*C*) plots. R4 is a contour gate including 99% of events. We combine the gates (Boolean AND) R1, R2, R4 and exclude R3 (Boolean NOT) that has been set on the TO^+ reticulocyte population. See Results[17] and the legend to Figure 5 for additional details on analysis.

[17] See Results>Morphometry>Light-scattering flow cytometry

Imaging flow cytometry (IFC). The imaging flow cytometer (ImageStreamX, Amnis Corporation, Seattle, WA) analyzes individual cells—in flow, by brightfield and multiple fluorescence parameters—as they flow past a 60× microscope objective. The device collects data as images, namely, two-dimensional spatial grids, with a third intensity dimension captured for each pixel. We load RBCs with CV (for viability), TO (for RNA), and DRAQ-5 (for DNA), as described above, and establish gating schemes in order to discriminate mature RBCs from other cell classes, measure $Ø_{Major}$ for biconcave disks and non-biconcave disks, and determine the proportion of the RBCs that are BCDs vs. nBCDs (see Results[18]).

Gating schemes (e.g., see Figure 6) that we establish allow size analysis of individual RBCs and RBC precursor types, separately from one another. Measurements of $Ø_{Major}$ are steps #6 (for BCDs) and #6′ (for nBCDs) in our workflow (see Figure 13), and determinations of fractional abundance are steps #11 (for BCDs) and #11′ (for nBCDs).

Use of inhibitors in imaging flow cytometry. As detailed in paper #1[19], we collect fresh blood from WT or KO mice, centrifuge, remove the buffy coat, suspend the pelleted RBCs in our oxygenated solution (see Table 1) to a hematocrit (Hct) of 5% to 10%, and then centrifuge at 600 × g for 5 min (see above[20]). After 2 such washes, we resuspend RBCs in oxygenated solution without drugs or with either pCMBS (1 mM for 15 min) or DIDS (200 μM for 1 hour), to a final Hct of 25%. After centrifuging RBCs at 600 × g for 5 min, we aspirate and discard the resulting

---

[18] See Results>Morphometry>Imaging flow cytometry

[19] See paper #1>Methods>Automated hematological analyses (workflow #7–#9)>Use of inhibitors in automated hematological studies

[20] See Methods>Preparation of RBCs>Processing of RBCs for assays 1–4

supernatant to remove inhibitors, and load the blood cells with CV, TO and DRAQ-5, as described above[21].

After implementing gating schemes (Figure 6) to sort mature RBCs from their precursors, we then sort the normal BCD RBCs from the nBCD cells, employing the Lobe count feature in the Ideas software, using the H Variance Mean function (granularity assigned as 5). This sorting procedure yields four bins of cells identified as possessing 1, 2, 3, or 4 lobes. Regardless of the lobe bin (i.e., 1, 2, 3, or 4 lobes), the majority of nBCD cells have H Variance Mean values <10. We manually inspect each cell in each bin of sorted cells to verify correct assignment of normal vs nBCD cells. We performed experiments on blood samples from 3 age-matched pairs of WT vs dKO mice.

Proteomic analysis

Preparation of RBC ghosts. We collect blood samples (0.2 to 0.5 ml) into heparinized microcentrifuge tubes from 3 mice for each genotype, and then place the tubes on ice, pending immediate processing into ghosts. We generate erythrocyte ghosts as previously described (Bennett, 1983), with the following changes to buffer composition (see Table 1): RBC lysis and post-lysis wash buffers contain 5 mM Tris-HCl/pH 8.0 and complete Protease Inhibitor Cocktail tablets (cPIC; Roche, 04693116001), as opposed to sodium-phosphate buffer/pH 7.5 and PMSF and pepstatin A—modifications required to obtain good mass-spectrometry data. Ghosts are then flash-frozen and held at −80 ˚C prior to mass-spectrometry analysis.

Mass spectrometry. We perform mass spectrometry experiments at the CWRU Center for Proteomics and Bioinformatics. Briefly, RBC ghost samples are lysed with 2% SDS and cPIC,

[21] See Methods>Flow cytometry (workflow #6 & #11)>Sample preparation

using pulse sonification, and removing SDS by filter-aided sample preparation (Wiśniewski, 2017) detergent cleanup. We determine total protein concentration using the Bio-Rad Protein assay kit (Bio-Rad, Hercules CA), digesting a 10-µg sample with LysC/Trypsin, and analyzing 300 ng of the resulting product via 24-hr label-free liquid chromatography–tandem–mass spectrometry (LC/MS/MS) using a UHPLC Vanquish LC system and a Orbitrap Exploris 480 Mass Spectrometer (TFS) following a previously described protocol (Schlatzer et al., 2009). We extract raw data from each run to generate MS/MS peak lists for identification purposes, as well as intensity-based profile peak lists for quantification using Peaks software (Bioinformatics Solutions, Ontario Canada). We perform one-way ANOVA to test for statistically significant differences in abundance (see below[22]).

Relative abundance. We determine relative abundance by comparing the mean area under curve (AUC) for all detected peptides for each protein, from 3 mice of each genotype. For example, for anion exchanger 1 (AE1; band 3; SLC4A1), we detect 57 different peptides. Therefore, in samples from 3 animals, the relative abundance of AE1 is the mean AUC of the 57 × 3 = 171 total peptides.

Statistical analysis

We report results as mean ± SD. In each figure legend, we report which statistical tests is performed, from among the following, to generate unadjusted p-values: (1) paired two-tailed t-test, (2) unpaired two-tailed Welch's t-test (Welch, 1947) or (3) one-way analysis of variance (ANOVA). For comparisons of 2 means, we performed #1. For comparisons among >2 means, we performed #2 or #3 and then, to control for type I errors across multiple means comparisons, we

[22] See Methods>Statistical analysis>one-way analysis of variance (ANOVA)

applied the Holm-Bonferroni correction, setting the familywise error rate (FWER) to $\alpha = 0.05$. Briefly, we order the unadjusted *P*-values for all N comparisons in each dataset from lowest to highest. For the first test, we compare the lowest unadjusted p-value to the first adjusted α value, α/N. If the null hypothesis is rejected, then we compare the second-lowest p-value to the second adjusted α value, $\alpha/(N-1)$, and so on. If, at any point, the unadjusted p-value is $\geq$ the adjusted α, the null hypothesis is accepted and all subsequent hypotheses in the test group are considered null.

Data availability

The data supporting the findings of this study are available within the paper and its Supplementary Information files. Any further relevant data are available from the corresponding author upon reasonable request.

Results

As described in Methods[23], we prepare RBCs from WT and AQP1-KO, RhAG-KO,-and dKO mice to assess the impact of each genetic deletion on RBC shape and other morphometric parameters, as well as on the RBC-membrane proteome. These data allow us to correlate the physiological data (i.e., SF) and automated-hematology data from paper #1[24], with mathematical modelling/simulations from paper #3[25] and thereby estimate P_{M,O_2}.

Morphometry

Blood smears

Effect of gene deletions. Expert review[26] of 12 blood smears for control cells (i.e., not treated with drugs) reveals unremarkable RBC morphology (Figure 1) of each of four genotypes: WT, *Aqp1*–/–, *Rhag*–/–, and *Aqp1*–/–/*Rhag*–/–, all on a C57BL/6_{Case} background. We observed only occasional target cells and stomatocytes, with no differences among genotypes. Previous authors noted normal RBC morphology for RhAG-KO mice (Goossens *et al.*, 2010).

Effect of drugs. Previous reports indicate that exposing RBCs to pCMBS does not change RBC shape (Kuchel *et al.*, 1997), whereas DIDS exposure can cause alterations in cell

---

[23] See Methods>Preparation of RBCs

[24] See paper #1>Results>Effect of pCMBS or DIDS on O_2 offloading from RBCs & ..>Effect of genetic deletions on O_2 offloading from RBCs & ..>Hematological and related parameters>Automated hematology

[25] See paper #3>Results

[26] by board-certified hematologist and co-author HJM

morphology (Mosior *et al.*, 1992; Blank *et al.*, 1994; Hoefner *et al.*, 1994). In the present study, in which we evaluated RBCs from WT and dKO mice, we determine (1) whether pCMBS or DIDS impact morphology of RBCs used in our SF experiments in paper #1, and (2) the extent to which drug-induced shape changes correlate with WT vs. dKO mice.

At the level of blood smears, we observe no remarkable drug-induced changes in RBC morphology for WT or dKO (Figure 2). In the particular case of pCMBS-treated cells, we note a faint halo of light-purple around cells. Occasionally, we observed vacuoles at the periphery of RBCs—outside of the cell membrane—in some of the pCMBS-treated samples (Figure 2, center panels). Expert review deems these changes to be artifactual, and likely to be related to the effect of the added pCMBS on the staining reactions.

Imaging of living, tumbling RBCs

The preceding analyses were performed on air-dried blood smears. In order to evaluate RBC morphology in an environment more closely approximating that of the SF reaction cell during k_{HbO_2} experiments, we also use DIC microscopy to observe living RBCs—suspended in our oxygenated solution (see Table 1) at an initial Hct of 25–30%—as we drop the RBC suspension onto glass coverslips overlaid with the same oxygenated solution (for a final Hct of 0.5–1%; see Methods[27]). We record both still and video micrographs of living RBCs as, driven by gravity, as they tumble through the focal plane and toward the coverslip surface, avoiding acquiring images at the coverslip surface because many quickly deform on contact with the acid-washed glass.

Effect of gene deletions. Still images from DIC microscopy (Figure 3) reveal that virtually all cells, regardless of the genotype of the donor mouse, are normal BCDs. In addition,

[27] See Methods>Still microphotography and microvideography of living RBCs

videos of living RBCs tumbling through our oxygenated solution (see Table 1)—see Video 1, Video 2, Video 3, and Video 4—confirm that nearly all RBCs of all four genotypes are normal BCDs.

Effect of drugs. DIC microscopy of inhibitor-treated RBCs (Figure 4 reveals that pCMBS pretreatment tended to cause the appearance of small, more spherical cells with spicules (Figure 4; yellow arrows), which we classify as nBCDs. The nBCDs were more prevalent in DIDS-treated than in pCMBS-treated cells.

Note that, in SF experiments on drug-treated cells, the RBCs usually entered the SF device within 5 min. For DIC experiments, this delay was typically 30-90 min. Thus, to the extent that formation of nBCDs is time dependent, the nBCD abundance observed by DIC would overestimate the actual abundance in SF experiments.

Light-scattering flow cytometry

Flow cytometry provides a more efficient and less subjective approach than microscopy for assessing the morphology of large numbers of living cells in an environment that resembles the SF reaction cell. In light-scattering flow cytometry, the amount of light scattered depends on both cell size and the cell's internal intricacy as the single cell passes through the laser beam. Simultaneous forward and side scatter have long been used in flow cytometry to discriminate among RBCs and various type of leukocytes.

Gating. To separate RBCs from very small particles on the one hand and aggregates on the other, we gate the light-scattering data—representing a total of >500,000 cells per run—by plotting FSC-A vs FSC-H. In Figure 5*A*, the thin cluster of gray points nearest the origin y-axis represents particulates ("P"), whereas the larger, diffuse cluster of gray points centered around FSC-A ~10^5 represent aggregates ("A"). We discriminate among RBCs, reticulocytes, and nucleated precursors by using gating schemes based upon staining with the fluorescent markers

CV, DRAQ-5 and TO (see Methods[28]). The tear-drop area ("R1") comprises the "gated" cells. For all four genotypes at least 99.9% of the cells within R1 are CV positive (i.e., viable). In Figure 5*A*, which is from one of the four WT samples, the arbitrarily-colored red pixels within R1 represent reticulocytes, whereas the arbitrarily-colored cyan pixels represent nucleated precursors or other nucleated contaminant cells. These colors are retroactively applied to the Figure 5*A* graph after we perform the additional gating steps described in Figure 5*B* and Figure 5*C*.

We subdivide the immature precursor cells into (1) nucleated precursors or other nucleated contaminant cells (R5 in Figure 5*B*, cyan pixels in Figure 5*A* and Figure 5*B*) and (2) reticulocytes (red pixels in Figure 5*A*-*C*).

In Figure 5*B*, we plot TO vs. CV intensity for the cells from R1 in Figure 5*A*. The small cluster of cyan pixels in the upper right of the plot are nucleated (DRAQ-5^{+}) cells and are gated as "R5" because of their strong DRAQ-5^{+} signal in Figure 5*C*. The remaining cells are gated as "R2". In Figure 5*C* we plot TO vs. DRAQ-5 intensity for the cells in R1 from Figure 5*A.* The cyan pixels on the top right of the plot represent the strongly TO^{+} and DRAQ-5^{+} cells that have both ER and nuclei. We then use Boolean gating to subtract the manually set region, R3 from the contour fit of the gray pixels in R4 (dashed box) to isolate the reticulocytes (for which the pixels coordinates are colored red) that have high TO signals but are DRAQ-5^{dim}[29] because they possess residual ER (with RNA) but no nucleus from the mature RBCs that lack both endoplasmic reticulum (ER) and nucleus, 99% of which are captured within the contour fit within R4.

---

[28] See Methods>Flow cytometry (workflow #6 & #11)>Sample preparation

[29] We define DRAQ-5^{dim} staining intensity as increased when compared to the negative control but $<10^{-4}$

Using these criteria we conclude that 97.1 ± 1.2% of the cells in the samples from the 4 WT animals in Figure 5*D* (green column) are mature RBCs.

Figure 5*D* also shows that the mean %RBC in AQP1-KO, RhAG-KO, and dKO samples is 96.9 ± 0.6% (pink column), 96.2 ± 1.2% (blue column) and 95.6 ± 1.4% (purple column) respectively. We further conclude that there are no substantial or significant differences between WT and any of the three KO strains in the percentage of each cell sample represented by reticulocytes (Figure 5*E*) or nucleated cells (Figure 5*F*).

Size and shape analysis. We next confine our light-scattering analyses to include only the gated mature RBC population (as defined in Figure 5*A*-*C*). Our goal is to identify any unexpected strain-dependent changes in size and/or shape that could potentially impact k_{HbO_2}, independent of P_{M,O_2}. Figure 5*G* and Figure 5*H* are respectively representative Boolean gated single parameter frequency distributions of the FSC-A/FSC-H and FSC-W from the single WT sample in Figure 5*A*. The distribution in Figure 5*G* can be considered the equivalent to passing along the magenta diagonal arrow through the mature RBC coordinates within R1 of the FSC-A/FSC-H in Figure 5*A*.

The individual RBCs from WT, AQP1-KO, RhAG-KO, and dKO have a uniform shape, as shown by the absence of any notable variations in the mean FSC-A/FSC-H ratio in Figure 5*I* or FSC-W in Figure 5*J* across all 16 animals (4 per strain) collectively. Overall, light-scattering analyses suggest that differences in the shapes of RBCs among the four genotypes are neither significant nor substantial. The small sample-to-sample variations among replicates (from 1 genotype) may be due to flow nuances (e.g., slight variation in flow rates), or environmental variables (e.g., small differences in cell density).

Imaging flow cytometry (IFC)

Whereas the light-scattering/fluorescence experiments, just discussed, provide a semiquantitative measure of cell size (FSC-H), cell size and shape (FSC-A), and cell classification (gated by fluorescent markers), IFC provides similar basic information as well as the high-resolution, multi-spectral imaging capability (see Methods[30]). As a result, we can observe the size and shape characteristics of individual RBCs, in flow. Similar to light-scattering flow cytometry, IFC allows the sorting (i.e., gating) of multiple cell classes based upon combinations of fluorescent markers, but adds concurrent brightfield image acquisition of individual cells as they pass a 60× microscope objective lens. Thus, the investigator can analyze cell size and shape, with substantially increased throughput and considerably reduced opportunity for subjective bias during analysis versus DIC microscopy, micrographs, or videography.

Effect of gene deletions. Using the same staining protocols as for the light-scattering flow cytometry (see Methods[31]), we label blood samples with CV, TO and DRAQ-5, and then establish gating schemes to sort the mature RBCs from reticulocytes, and nucleated precursors or other nucleated contaminant cells.

Figure 6*A* is a frequency histogram for a one of four IFC runs on WT material, representing all CV^+ events (i.e., viable cells), plotted as a function of TO (i.e., RNA) intensity. We represent the TO^+ events—about 15,000 (i.e., ~4.5% of the total events), distributed across a span of 999

---

[30] See Methods>Flow cytometry (workflow #6 & #11)>Imaging flow cytometry (IFC)

[31] See Methods>Flow cytometry (workflow #6 & #11)>Light-scattering flow cytometry

bins along the x-axis—as peach dots and line segments. The ~350,000 (i.e., >95% of the total events) TO^- events. fall within a single bin (green).

In Figure 6*B*, we analyze just the TO^+ events by plotting projection area of the imaged event vs. bright-field aspect-ratio intensity[32]. The burgundy events represent single TO^+ cells. The gray events in the upper left are particulates ("P"), whereas the dull-olive events to the center/right are aggregates ("A").

In Figure 6*C*, we analyze just the TO^+ single cells by plotting the brightfield area of the imaged event vs. DRAQ-5 aspect ratio intensity[33]. The events colored purple are single TO^+ (RNA^+)/DRAQ-5^+ (DNA^+) cells that could be nucleated RBC precursors or other nucleated cells (e.g., contaminating white blood cells), neither of which would contain hemoglobin (i.e., they would not affect SF experiments in paper #1). The orange events that appear to from a line at $y \cong 0$ are TO^+ (RNA^+) but DRAQ-5^- (DNA^-). These are reticulocytes.

Returning to Figure 6*A*, we now analyze just the TO^- (RNA^-) events (green) by plotting in Figure 6*D* brightfield area (analogous to Figure 6*B*) vs. the brightfield aspect ratio intensity. The events colored pink in Figure 6*D* represent TO^- single cells that lack RNA (i.e., RBCs). The gray events in the upper left are TO^- particulates ("P"), whereas those colored dull-olive to the center/right are TO^- aggregates ("A").

---

[32] The ratio of the minor axis to the major axis of an object, calculated based on the intensity of the pixels within the object in the brightfield image (Channel 1).

[33] The ratio of the minor axis to the major axis of an object, calculated based on the fluorescence intensity of the pixels within the object in channel 11.

Finally, in Figure 6*E*, we analyze just the single TO^- (RNA^-) cells by plotting the brightfield area of the imaged event vs. the fluorescence aspect ratio intensity which is >0 if there are contaminating SpeedBeads™[34] in the image. The blue-colored events represent single, mature RBCs in which a SpeedBead™ appears in the same image. Finally, the red events that appear to from a line at $y \cong 0$ represent single, mature RBCs that are uncontaminated by SpeedBeads™.

Of the ~375,000 images that generate the data for the WT sample in Figure 6*A–E*, Figure 6*F–G* are exemplars of two classes, reticulocytes and nucleated cells. Figure 6*F* is a data collage of four reticulocytes, and Figure 6*G* is the same for nucleated cells. In each panel, each of the four data rows contains comprises a brightfield image of the cell in flow, a TO image (green, RNA^+), a CV image (gray, viable), and DRAQ-5 image (red, DNA^+).

The data summarized in Figure 6*A–E* are one of four IFC runs on WT mice. The top data row in Table 2 summarizes data for all four WT runs—the abundance of single mature RBCs, reticulocytes, and nucleated cells.

Data rows 2–4 in Table 2 summarize comparable data for the three KO strains. We see a trend for the abundance of mature RBCs to slightly decrease in the order WT > AQP1-KO > dKO > RhAG-KO with an almost reciprocal increase in the reticulocyte percentages in the order WT < AQP1-KO < dKO < RhAG. We also see small increases in the percentage of nucleated cells in the order WT < AQP1-KO < RhAG-KO < dKO. The box-plot in Figure 6*H* displays in more detail the individual results from each of the four runs for each genotype summarized in Table 2. Figure 6*H* highlights the trend for increased reticulocyte (left-grouped box plots) or nucleated cell (right-

[34] The ImageStream system uses the SpeedBeads™ scatter signal to monitor and synchronize the flow of the sample, as well as to maintain focus and core tracking (Cytek Biosciences, 2024).

grouped box plots) percentage in each of the KO strains. However, neither the increases in the percentage of reticulocytes nor in the proportion of nucleated cells in KO blood are statistically significant compared with WT.

The major advantage that IFC offers over conventional flow cytometry is the opportunity for the user, in brightfield images, to assess individually the morphology of hundreds of thousands of RBCs and directly measure their $Ø_{Major}$ (Figure 6*I*, red box). We find that $Ø_{Major}$ is slightly smaller in KOs than WT (Table 3) for either mature RBCs alone, or "all cell types" (i.e. mature RBCs + reticulocytes + nucleated cells). These results imply, together with increased MCVs for the KO strains (Table 4), that KO cells are slightly thicker. Due to the extremely high number of individual cells analyzed, one-way ANOVA with a Holm-Bonferroni means comparison (Holm, 1979; see Methods[35]) shows that differences between all pairs of mean $Ø_{Major}$ values are statistically significant ($P<0.001$ for all comparisons). However, even the greatest difference (i.e., between WT and RhAG-KO) among only mature RBCs is ~5% (i.e., 6.79 μm vs. 6.47 μm), and for "all cell types" (i.e., the sum of mature RBCs + reticulocytes + nucleated cells) is <5% (i.e., 6.80 μm vs. 6.53 μm). In our mathematical modeling in paper #3, we take as the diameter, the diameter of "all cell types." This approach reflects the reality of an SF experiment (paper #1), which necessarily includes all cell types. Note that the inclusion of larger-diameter RBC precursor cells in the size analyses, does not substantially increase the mean major blood cell diameter because these precursors represent only 4% (WT) to 7% (RhAG-KO) of the total cells in the sample.

Effect of drugs. IFC shows that under control (no-drug) conditions, nBCDs account for only ~1.4% of cells among WTs, and ~2.5% in dKOs (Table 5). These percentages are consistent

[35] See Methods>Statistical analysis

with our observation of spherical cells or cells with spicules by DIC microscopy/videography are rare (see above[36] and Figure 3). IFC brightfield images (Figure 7*A*) reveal that the nBCDs are a mixture of poikilocyte types, mainly echinocytes, acanthocytes and spherocytes.

In cells from WT mice, nBCDs rise from ~1.4% of the total count under control conditions to ~8.7% after 15 min pretreatment with 1 mM pCMBS (Table 5), and to ~41% after 1 h pretreatment with 200 μM DIDS (see Figure 7*B* and Table 5). The drug-treated percentages are far lower for blood from dKO mice: only ~5.7% with pCMBS pretreatment (~35% lower vs. WT), and only ~21% with DIDS pretreatment (~48% lower vs. WT; see Figure 7*C* vs. *B* and Table 5). We used the mean $Ø_{Major}$ values and the percentages of BCD vs. nBCD cells in each condition in mathematical modeling (see paper #3) to take into account the contribution that the inhibitor-induced changes in RBC morphology have on k_{HbO2}.

Proteomics

Because the genetic deletion of one protein could alter the expression of others, we assessed effects of the KOs on RBC membrane-protein levels by generating RBC ghosts, isolating the proteins, and quantitating them by mass spectrometry (label-free LC/MS/MS). We determined the apparent abundance of 7,188 unique peptides from 1105 total proteins, not all of RBC origin, including 212 plasma-membrane–associated proteins (PMA proteins; Supporting file 1).

Validated deletion of targeted proteins in knockout strains. Our three strains with genetic deletions—*Aqp1–/–*, *Rhag–/–*, and *Aqp1–/–Rhag–/–* (i.e., the dKO)—produced the expected elimination of the cognate proteins from RBC membranes, namely, AQP1 (Figure 8*A*) and RhAG (Figure 8*B*). In addition, the deletions of *Rhag* in the RhAG-KO and dKO also

[36] See Results>Morphometry>Imaging of living, tumbling RBCs

eliminated RhD (Figure 8*C*), which forms heterotrimers with RhAG (Gruswitz *et al.*, 2010) and falls pari passu with RhAG. We describe the vastly smaller effects of the knockouts on the abundance of other individual proteins below.

PMA proteins with highest inferred abundance and the major macromolecular complexes into which they assemble in WT RBC ghosts. Among the 50 total proteins with the greatest inferred abundance, 22 are PMA proteins (Table 7). Figure 9 displays the abundance of the unique peptides from the top 22 PMA proteins in WT RBC ghosts. These 22 proteins span a ~40-fold range in inferred abundance. As can be seen by totaling the numbers in the appropriate columns in Table 7, the 22 proteins comprise ~87% of PMA protein abundance in WT ghosts, and ~42% of total protein abundance. The 25 PMA proteins with the next-highest apparent abundance—also listed in Table 7—collectively comprise just an additional ~5.7% of PMA protein abundance in WT ghosts, and ~2.8% of total protein abundance. Thus, a relatively small number of proteins represent an overwhelming fraction of protein variety associated with the RBC membrane from WT mice.

The predominant protein is AE1 (represented by 57 unique peptides; a total of 171 peptides from the analysis of three WT mice), which, by itself, comprises ~9.5% of the total WT RBC ghost proteome in our dataset, and ~20% of all the identified WT PMA protein content (Table 7).

The second most abundant PMA protein is glycophorin A (GYPA), which facilitates AE1 cell-surface expression (Groves & Tanner, 1992, 1994; Pang & Reithmeier, 2009; Hsu *et al.*, 2022) and comprises ~9% of the total WT RBC ghost proteome, and ~19% of all PMA protein content (Table 7). Collectively, murine RBC proteins that correspond to components of the human ankyrin-1 "complex a", for which Vallese *et al.* (2022) determined the atomic structure, comprise ~62% of all PMA proteins that we detect (see Table 7): AE1 (19.6% of PMA proteins), GYPA (18.6%), AQP1 (~8.25%), ankyrin-1 (ANK1, 4.25%), spectrin β (SPTB, 3.73%), RhAG (3.23%), erythrocyte membrane protein 4.2 (EPB42, 2.97%), and RhD (1.78%).

Collectively AQP1–the only AQP species detected in the murine ghosts in these analyses–and the Rh_{Cx}, the proteins targeted in our KO strains (indirectly in the case of RhD), comprise ~13% of the WT RBC ghost PMA proteins. All of them are among the top 13 most abundant PMA proteins (see Figure 9) and top 24 in overall abundance (see Supporting file 1).

AE1, and RhAG also associate the plasma membrane with the cytoskeleton via interaction with erythrocyte membrane protein 4.1 (EPB41) in a second macromolecular protein complex that includes glycophorin C (GYPC), atypical chemokine receptor 1 (ACKR1; Duffy blood group antigen), the endoplasmic reticulum membrane adapter protein XK, and the zinc endopeptidase Kell blood group glycoprotein homolog (KEL; Bennett, 1983; Reid *et al.*, 1990; Marfatia *et al.*, 1994; Nicolas *et al.*, 2003; Salomao *et al.*, 2008; Suzuki *et al.*, 2014). The contributions of each component of the murine "protein 4.1 complex" to the RBC ghost proteome are displayed in Table 7. Collectively, AE1, Rh_{Cx}, EPB41, GYPC, XK and KEL comprise 33.7% of the PMA proteins. Due to the ability of mice to synthesize their own vitamin C (Chen *et al.*, 2012), the glucose transporter type 1 (GLUT1; SLC2A1), a constituent of the human "protein 4.1 complex" is not detected in mouse RBC ghosts (Rungaldier *et al.*, 2013). However, GLUT3 (SLC2A3) is present, constituting approximately 0.1% of the PMA protein.

Stomatin (STOM; also known as lipid raft protein band 7) is a scaffolding protein that oligomerizes in RBC cholesterol-rich lipid rafts, modulates ion channels and transporters and is known to interact with several of the key components of the ankyrin and protein 4.1 complexes detected in the mouse RBC ghosts in this investigation including, AE1, AQP1, RhD, and EPB42 (Rungaldier *et al.*, 2013). Other known STOM interacting proteins detected in this study include the urea transporter 1 (UT-B; SLC14A1) that also behaves as an NH_3 channel (Geyer *et al.*, 2013), and which constitutes ~0.8% of RBC PMA protein (Table 7), and the flotillin-1 (FLOT1) and flotillin-2 (FLOT2) scaffolding proteins (collectively ~0.016% of RBC PMA protein).

Inferred abundance of other PMA transporter or channel proteins in the WT RBC ghosts. Besides AE1, the other 23 detected PMA SLC proteins represent only ~3% of the total RBC proteome and ~5% of the PMA protein content (Table 8). The most abundant of these 23 SLC proteins is the monocarboxylate transporter 1 (MCT1; SLC16A1), with 10.5-fold lower expression than AE1, comprising ~2% of the PMA proteins.

Combined, 0.276% of the PMA protein comes from the ATP1A1 (0.096%; Supporting file 1), ATP1B2 (0.167%; Table 7) and ATP1B3 (0.013%; Supporting file 1) Na^+/K^+ ATPase subunits, whereas the plasma membrane Ca^{2+}-transporting ATPase 2 (ATPB2) constitutes ~0.2% of the PMA protein in WT RBC ghosts (Table 7). The phospholipid-transporting ATPase 11C (ATP11C)–the catalytic component of a P4-ATPase flippase complex in the RBC plasma membrane that is critical for retaining phosphatidylserines (PS) within the inner leaflet and preventing surface exposure (Yabas *et al.*, 2014)–constitutes 0.04% of the PMA protein in WT RBC ghosts (Supporting file 1).

Other detected PMA proteins with permanent pores are low in abundance and include the ion channels piezo-type mechanosensitive ion channel component 1 (PIEZO1; 0.0736%)—PIEZO1, the protein that defines the Er-blood group (Karamatic Crew *et al.*, 2023)—found in both endoplasmic reticulum and the plasma membrane subcellular compartments (Coste *et al.*, 2010; Fang *et al.*, 2021), and the transient receptor potential cation channel subfamily V member 2 (TRPV2; 0.0599%), which together account for <0.14% of the RBC PMA protein (Belkacemi *et al.*, 2021). PIEZO1 ranks #305 in abundance among all WT RBC proteins and #79 among PMA proteins. TRPV2 is the 329th most abundant RBC protein overall and #90 among PMA proteins (Supporting file 1).

Effect of knockouts on abundance of individual proteins. Among the 22 PMA proteins with greatest inferred abundance in WT ghosts (see Figure 9), none are detected with significantly altered levels in response to the deletions of *Aqp1* and/or *Rhag*. Figure 10

summarizes, for each of the three KO genotypes, the fold changes (normalized to WT) for each of these 22 PMA proteins. Neither do any of the next 25 most abundant PMA proteins (see Table 7) exhibit a significant change in inferred abundance in response to single or double gene deletions (see Supporting file 2).

We find that only 27 out of 1105 proteins—16 non-PMA proteins and 11 PMA proteins—in the RBC-ghost preparation exhibit a significant change with at least 1 genetic deletion (Figure 11). Of these, the protein with the greatest inferred abundance is a non-PMA protein, proteasome subunit α type-4 (PSMA4), a subunit of the 20S core proteasome complex that is present in RBCs (Kakhniashvili *et al.*, 2004; Majetschak & Sorell, 2008; Neelam *et al.*, 2011; Tzounakas *et al.*, 2022), ranking #101 in WT ghosts, exhibits a significant ~38% lower abundance in the AQP1-KO (Figure 12). The #133 ranked protein, proteasome subunit α type-1 (PSMA1), also exhibits a significant ~31% reduction in abundance compared to WT in the AQP1-KO RBC ghosts (Figure 12). However, the inferred abundance (Table 9) for both PSMA1 & PSMA4 proteins are <1% that of the #1 protein, AE1 (see Table 7).

Among PMA proteins exhibiting significant changes, the integrin ITGA2B has the highest inferred abundance, which ranks #136 overall (0.07% of all proteins) and #48 (0.15%) among PMA proteins (Table 10). It is prevalent in platelets, rather than mature RBCs (Nurden, 2021). ITGA2B peptide abundance significantly increases in AQP1-KO and RhAG-KO samples, but decreases in the dKO samples (Figure 10*E*), most likely reflecting small differences in platelet contamination in our ghost samples rather than atypical ITGA2B expression in erythrocyte membranes.

Consequently, we establish a quantitative threshold, below which we deem any statistically significant changes in PMA protein expression as inconsequential for identifying the essential candidate proteins that influence RBC P_{M,O_2}. In both the AQP1-KO and dKO, the detected background abundance signal for AQP1 represents 0.05% of the PMA protein RBC proteome (and

~0.02% of the total RBC proteome; Supporting file 1). The gray shaded rows in Table 8 and Table 10 highlight the sub-threshold protein species according to these criteria, and of the 11 PMA proteins with significant differences in their inferred abundance in our proteomic analysis of either single KO or dKO mice (Figure 12), only ITGA2B, NRAS, and ADAM10 are above this threshold 0.05% of the total PMA protein in WT RBCs (Table 10). Even then, the significant differences in ITGA2B expression in the KO mice are most likely attributable to differences in residual platelet contamination in the samples (Nurden *et al.*, 2011), differences in NRAS are most likely from hematopoietic and progenitor cells (You *et al.*, 2021) and ADAM10 from WBCs (Pruessmeyer *et al.*, 2014; Lambrecht *et al.*, 2018; Zingoni *et al.*, 2020).

Discussion

This study particularly characterizes the morphologies and proteomes of murine RBCs for our lab-standard WT strain, C57BL/6_{Case}, as well as AQP1-KO, RhAG-KO, and dKO mice, all on the same genetic background. We conclude that neither RBC morphology nor PMA protein abundance—aside from the proteins specifically affected in the KO models—exhibit significant variations in the KO animals, so excluding these variables as possible contributors to the k_{HbO_2} differences noted in paper #1, and providing the necessary experimentally determined parameters for the modeling in paper #3

We use mice as a surrogate for human RBC in this work to facilitate the genetic knockout of our candidate gas-channel proteins. However, it is important to note that mouse RBCs differ from human RBCs in several key aspects. Mouse RBCs are generally smaller than human RBCs, have a shorter lifespan—typically around 55 days, compared to the 120-day lifespan of human RBCs—and the shape of mouse RBCs can also vary more than human RBCs that are more consistently biconcave (Gilson *et al.*, 2009; O'Connell *et al.*, 2015). Furthermore, the hemoglobin content and oxygen-carrying capacity is higher in humans than mice (Russell *et al.*, 1951; Webb *et al.*, 2021), and even varies between different mouse strains (See table 1 in Russell *et al.*, (1951)), reflecting adaptations to their distinct physiological needs and environments. Mice also have relatively more circulating reticulocytes and platelets than humans (O'Connell *et al.*, 2015).

Morphometry

Morphology

Our work with blood smears (Figure 1) and imaging of living, tumbling RBCs (Figure 3) indicate that the RBCs from mice with genetic deletions in *Aqp1* and or *Rhag* are morphologically indistinguishable from those from WT mice. Our data align with previous reports that erythrocyte morphology is unaltered in AQP1-KO and AQP1/UT-B dKO mice (Yang & Verkman, 2002), and

that AQP1-deficient (Colton-null) human RBCs are morphologically identical to *AQP1*+/+ human RBCs (Mathai *et al.*, 1996). Similarly, our findings align with other microscopic analyses that determined that there are no major morphological differences between of RhAG-KO and WT RBCs (Goossens *et al.*, 2010). We are the first to study the morphology of AQP1/RhAG dKO RBCs. The proportion of RBCs that are nBCDs from each genotype or in the presence of pCMBS or DIDS is addressed below in our discussion of IFC.

Flow Cytometry for qualitative and quantitative analyses of blood cell morphology

IFC has been employed in parasitology to classify by size, erythrocyte-derived microvesicles in human malaria infections (Mantel *et al.*, 2013), or to screen for compounds that destabilize the *P. falciparum* digestive vacuole (DV; Lee *et al.*, 2014). IFC has also been used to demonstrate that RBCs are the predominant blood cell type infected by *Brucella melitensis* (Vitry *et al.*, 2014). IFC can also be used to classify and count erythroid progenitors to delineate the stages of erythropoiesis (McGrath *et al.*, 2017; Kalfa & McGrath, 2018), characterize the magnetic susceptibility of human monocytes (Kim *et al.*, 2019), or to ascertain whether the substantially elevated platelet counts observed during *ex vivo* lung and liver xenografts originate from RBC fragmentation into platelet-sized particles (Habibabady *et al.*, 2022).

Several studies measure the dimensions and morphology of fixed human RBCs and morphologic homogeneity using IFC. Fixed human RBCs imaged in the bright-filed channel were measured for compactness, circularity, aspect ratio, and shape ratio and dimension (surface area, and perimeter under control conditions and after lysophosphatidylcholine (LPC) treatment which induces echinocytosis and eventually spherocyte formation (Safeukui et al., 2012) or *P. falciparum*-infection (Safeukui et al., 2013). In the above investigations, the distribution of measured human RBC $Ø_{Major}$'s in control conditions centered on 9-10 μm. Another group also demonstrated

that patients with severe malaria have RBCs with 8.9% smaller projected surface area after Artesunate treatment, induces ejection of the parasite (Jauréguiberry et al., 2014).

Some studies use IFC to quantify they proportion of echinocytes, sphero-echinocytes, and spherocytes in stored non-fixed human RBC samples (Pinto *et al.*, 2019; Marin *et al.*, 2022). But to the best of our knowledge, we are the first to employ the IFC to compare RBC morphology between wild-type and different strains of KO mice. In this investigation, we focus on live murine RBCs (not fixed) and found no remarkable differences in RBC morphology, particularly $Ø_{Major}$, between the WT and the three KO mouse strains either by light-scattering flow-cytometry or IFC.

nBCDs (poikilocyte) abundance. While the morphological analyses in this study were performed to determine the contribution that the genetic and inhibitor-induced changes in RBC morphology have on k_{HbO2}, we also ascertain that the nBCD abundance in the WT and dKO strains is extremely small (<3%). Furthermore we determine that pCMBS- and DIDS- pretreatment induces significantly increased poikilocytosis (Table 5).

pCMBS- and DIDS-mediated inhibition of ion transport via AE1 and water transport via AQP1 disturbs the Gibbs-Donnan equilibrium (Gibbs, 1878; Donnan, 1911), modulating osmotic pressure across the plasma membrane, causing alterations in RBC morphology. The transition from BCDs to echinocytes (Burr cells) is reversible (Wong, 2018), but prolonged incubation with inhibitors promotes irreversible poikilocytosis.

Because the mercurial agent pCMBS is generally considered membrane-impermeable, it primarily interacts with cysteine residues in membrane proteins that are accessible from the extracellular side of the cell membrane (Benga et al., 1986), thereby inhibiting membrane transport, which results in mild effects on RBC morphology. This contrasts with Hg, which can significantly disrupt the typical biconcave disc shape of red blood cells. This disruption occurs not only due to its inhibition of water and substrate transport through PMA proteins but also because

it penetrates the plasma membrane, reacting with intracellular and cytoskeletal thiols that are essential for the association of AE1 with spectrin β through ankyrin (Vallese *et al.*, 2022; Notariale *et al.*, 2022). The morphological impact of pCMBS is therefore milder than Hg.

The impact of DIDS incubation on RBC morphology is likely substantially more pronounced compared to that for pCMBS (Figure 7, Table 5) because in addition to inhibiting substrate transport, DIDS forms cross-links between AE1 dimers through their extracellular Lys residues, leading to an increase in the surface area contact between the dimers and the surrounding lipid, while also severing their association with the cytoskeleton (Cabantchik & Rothstein, 1974*a*, 1974*b*; Hsu & Morrison, 1983; Van Dort *et al.*, 2001). Furthermore, DIDS-crosslinking inhibits the conformational transitions required for AE1 function (Capper *et al.*, 2023) that through its interactions with ankyrin and spectrin β normally controls cytoskeletal contraction and relaxation, plasma membrane tension and reversible RBC shape deformations, leading to poikilocytosis (Wong, 1994, 2004).

AE1 is not the sole target of DIDS in the RBC; DIDS also crosslinks AQP1 monomers within each AQP1 tetramer, thereby inhibiting its permeability to CO_2 (Boron & Cooper, 1998; Endeward *et al.*, 2006; Musa-Aziz *et al.*, 2007*b*, 2007*a*, 2025; Geyer *et al.*, 2011). In a similar manner, DIDS reduces CO_2 permeability through RhAG (Endeward *et al.*, 2008). Considering that both AQP1 and RhAG are integral components of the ankyrin complex (Vallese *et al.*, 2022), it is reasonable to predict that DIDS-crosslinking of either AQP1 and/or RhAG in conjunction with AE1, will exacerbate the morphological transition from BCDs to poikilocytes. This crosslinking is likely to impede the conformational transitions of AQP1 and RhAG related to substrate transport, while concomitantly restricting the flexibility of the cytoskeleton to which both channels are coupled. It is evident in our experiments that the impact following both pCMBS and DIDS incubation on dKO RBC morphology, which express AE1 but not AQP1 and RhAG, is significantly less severe in comparison to that observed in WT red blood cells (Figure 7).

Nonetheless, due to the longer interval between drug treatment and IFC tests (~30-90 min) compared to the interval between drug treatment and SF trials (~5 min), the nBCD abundance derived from IFC studies likely a worst case scenario, overestimating the true abundance seen in SF experiments. To our knowledge, our IFC study is the first quantitative search in physiological experiments for murine nBCDs, which nevertheless were presumably present in previous studies. In future studies, it would be valuable to determine the interrelationships among (1) drug concentration and exposure time, (2) decrease in P_{M,O_2}, and (3) nBCDs abundance, with the goal of determining protocols that maximize inhibition while minimizing nBCDs formation.

RBC geometry in flow cytometry vs in blood vessels Quantifying RBC morphology by IFC is an accurate method to determine $Ø_{Major}$ and nBCD abundance in order to determine RBC $P_{M,O2}$ derived from the SF experiments. Nonetheless, in the body, the majority of RBCs adopt a deformed morphology in narrow capillaries to facilitate passage due to the capillary lumens being narrower than the RBC $Ø_{Major}$ (Secomb, 2017). The alteration in shape allows RBCs to squeeze through the narrow capillaries and maximize O_2 delivery to tissues. Moreover, this deformation is reversible once the RBCs return to larger blood vessels, allowing them to regain their original shape only increasing their lumen diameter when O_2 demand increases (Hamilton *et al.*, 2010). High-resolution adaptive optics imaging for non-invasive monitoring of RBCs in live human tissue demonstrates that when large RBCs navigate small channels, they adjust their orientation to align with the flow axis. Furthermore, the cells elongate, the intercellular distances rise, and paradoxically, the cell volume diminishes (Bedggood *et al.*, 2024). This indicates that water is expelled from the RBCs—presumably in large part via AQP1 (Sugie *et al.*, 2018)—to aid their transit through the capillaries. However, while deformed, the k_{HbO2} of individual RBCs is almost certainly different from the canonical, non-deformed bi-concave disc, but we predict that the extent to which RBCs lacking AQP1 are able to deform will be less. Such *in vivo* morphological changes will be the subject of future investigations to determine the impact of RBC deformation on $P_{M,O2.}$

Non RBCs In addition to the %nBCDs and poikilocytes we determined that nucleated cells represent ~1.5% in WT, ~1.7% in AQP1-KO, ~2.5% in RhAG-KO and ~2.5% in dKO of all the cells counted by IFC. The samples will be a mixture of erythroblasts and some residual white blood cell (WBC). Erythroblasts, are nascent blood cells and adults seldom have them in their circulating blood. Nucleated RBC counts are often expressed as a percentage of total WBCs or as an absolute number RBC/μL or per liter ($\times 10^9$/L). Standard values are 0-0.5% nucleated RBCs as a percentage of total WBC and 0 to 1 per 100 WBC or 0-0.01$\times 10^9$/L. These values may vary slightly between laboratories, and nucleated RBC percentage also increases with age (Stachon *et al.*, 2002).

Because the WBC are largely removed by the early centrifugation steps during RBC sample preparation, the proportion of nucleated cells in our IFC samples is increased compared to what would be measured in whole blood, and for this reason we do not include them in the calculations of k_{HbO2} and $P_{M,O2}$ in paper #1, and paper #3, using only the parameters for the Hb containing cells (i.e. RBCs and reticulocytes).

Proteomics

Historical background.

Various RBC proteomic analyses from both humans and mice reveal numerous PMA proteins/protein complexes that likely contribute to transmembrane O_2 transport (Kakhniashvili *et al.*, 2004; Pasini *et al.*, 2006, 2008; Goodman *et al.*, 2007; Pesciotta *et al.*, 2012, 2012; Bryk & Wiśniewski, 2017; Gautier *et al.*, 2018; Vallese *et al.*, 2022), but the interactions among these proteins and their contributions to maintaining optimal k_{HbO2} remain under investigation. However, all these studies consistently indicate that AE1 (Band 3) is the predominant PMA transport protein, followed by the Rh_{Cx} proteins and AQP1 among the next most abundant PMA species.

The mouse RBC ghost proteome.

In our proteomic analyses of the RBC ghosts obtained from the WT and three KO mouse strains used in this study, inferred abundance from LC/MS/MS data refers to the estimation of the quantity of specific ions (or molecules) in a sample based on the detected signal intensity, and reports the relative abundance of proteins or peptides by measuring the ion counts or peak areas in the mass spectra. The main objective of conducting the proteomics was to confirm that the expression of the target proteins in each KO strain was effectively abolished, and whether there were any corresponding reductions or compensatory upregulation of other proteins in the RBC proteome of each KO strain.

In our analyses, we focused in particular on the plasma membrane-associated (PMA) proteins, which we define as proteins that are either embedded within the membrane (i.e. integral), attached to it directly (e.g., via a glycosylphosphatidylinositol anchor) or indirectly (e.g. a cytoskeletal protein such as ankyrin interacting with an integral membrane protein like AE1). In addition to genotype-specific differences in expression level, for PMA proteins with indirect association, the amount of protein detected in the ghost samples is also influenced by minor variations in wash step stringency. For high-abundance cytoskeletal proteins like ankyrin (Rank #9 overall and #5 in PMA proteins, Table 7) inter-sample variations resulting from minor differences in wash stringency have minimal impact. For low-abundance PMA species, such as the disks large homolog 1 (DLG1) scaffolding protein (Ranked #1069 overall and #208 in PMA proteins; Table 10), which is 850-fold less abundant than ANK1, minor variations in sample preparation are likely to cause a more substantial error in the measured abundance of the detected peptides and be responsible for any statistically significant fold-changes. However, much of the lowest-level detected protein in the ghost samples originates from non-RBC contamination in the sample (e.g. DLG1 in WBCs); hence, the influence of a single sample with an elevated proportion of non-RBCs might be substantial.

We exclude most possible variations in the expression of low-level identified proteins from consideration as important by setting a quantitative threshold based upon the abundance of the residual AQP1 signal in AQP1-KO and dKO ghosts. In doing so we observe that the only three PMA species are detected above this threshold that exhibit significant differences in expression in the KO samples vs WT (ITGA2B, NRAS and ADAM10), and all mostly likely arise from residual platelet, erythroblast or WBC contamination in the samples rather than from unusual RBC expression.

We therefore confirm that AQP1 and/or the RhCx are effectively and appropriately absent in AQP1-KO, RhAG-KO, or dKO RBCs, and that among the 22 proteins that comprise ~87% of the PMA protein in WT RBCs, that there are no other significant alterations in abundance (Figure 10). Thus, changes in abundance of membrane proteins other than AQP1 and RhAG/RhD are unlikely to contribute to the observed KO-induced decreases in k_{HbO_2} in paper #1.

PMA proteins contributing to $P_{M,O2}$.

Vallese *et al.*, (2022) recently determined the structural origination of the human erythrocyte ankyrin complex, the major RBC PMA protein complex that contributes to the stability and shape of the RBC membrane by tethering the via spectrin-actin cytoskeleton to the lipid bilayer. The "Class 1a" ankyrin complex contains three AE1 homodimers, one AQP1 tetramer, one Rh_{Cx} heterotrimer (2×RhAG/1×RhCG), GYPA, GYPB, and protein 4.2 anchored to the cytoskeleton via spectrin and ankyrin-1. In the Class 1a complex, "AE1-I" interacts via protein 4.2 with ANK1, whereas "AE1-II" and "AE1-II" directly bind ANK1 via their N-termini. The charged AQP1 N-terminal residues K7, K8 and R12 mediate its interactions with ANK1, and it is the RhCE that anchors the Rh_{Cx} to ANK1 in the complex via both its N- and C-termini. In murine RBCs, which do not express RhCE, this role is likely undertaken by RhD.

Vallese *et al.*, (2022) identified 6 other lower-order ankyrin complex subclasses (Class 1-6), which each contain at 1-3 AE1 homodimers and one $Rh_{Cx.}$ The inclusion of one AQP1 is variable. Class 1-6 are predicted to occur *in vivo* but they may be less prominent than under the conditions designed to stabilize the interactions for the Cryo-EM study. It is fascinating to speculate that in mature Class 1a ankyrin complexes (AE1-I-III +AQP1+Rh_{Cx}), that the component of P_{M,O_2} mediated by Rh_{Cx} for example, is modulated through the simultaneous transport activities AE1 and AQP1, because mechanical forces are transduced through their common spectrin-actin cytoskeletal anchor. Similarly, the pharmacological inhibition of transport activity by blocking one of the AE1, AQP1, or Rh_{Cx}, or the crosslinking of their extracellular domains, is expected to adversely affect P_{M,O_2} through the remaining two pathways. Moreover, P_{M,O_2} via AQP1 or Rh_{Cx} may differ markedly in the Class 2-6 ankyrin complexes compared to the Class 1a complex, and the efficacy of pCMBS- or DIDS-induced block be diminished because the interactions between the major constituents of $P_{M,O2}$ are less extensive than in the complete Class 1a complex. Under specific circumstances, the relative prevalence of these lower-order complexes vs. the Class 1a complex may significantly influence overall RBC P_{M,O_2}.

The absence of AQP1 and/or RhAG protein in APQ1-KOs, RhAG-KOs and dKOs, will substantially alter Class 1 (AE1-I-III +Rh_{Cx}) prevalence, and eliminate Class 1a complexes (AE1-I-III +AQP1+Rh_{Cx}). In AQP1-KO RBCs the ankyrin complexes will be distributed among Class 1, Class 3 (AE1 +Rh_{Cx}), Class 4 (AE1-I-III + Rh_{Cx} + an unknown protein) and Class 6 (AE1-I & III Rh_{Cx}). Because Rh_{Cx} is common all of the ankyrin complex classes described by Vallese *et al.*, (2022) it remains to be determined how AQP1 will assemble with AE1 in the RhAG-KOs and whether AE1 continues to cluster similarly via ankyrin in the absence of both AQP1 and RhAG/D.

It is probable that some weaker or more transient interactions with ANK1 might not have been captured in the cryo-EM structures due to their dynamic nature or lower binding affinity. CD-47 and ICAM4 (the Landsteiner-Wiener antigen, LW) are previously recognized constituents of

the ankyrin complex (Mankelow *et al.*, 2012) that were not detected in the complexes described by Vallese *et al.*, (2022). This suggests a loose association, either lost during digitonin extraction, or affiliation with a different complex that could not be isolated. CD47 and ICAM4 are both present in our murine RBC proteomes (Table 7 and Table 10) and the extremely low abundance of ICAM4 (#144 among PMA proteins) aligns with probable loss of that specific protein during ghost sample washing.

Similarly protein 4.1 (EPB41), which is present in almost equal abundance as protein 4.2 (EPB42) in our murine RBC ghosts (Table 7) but which is absent from the Vallese *et al.*, (2022) complexes, likely plays an important role in different complexes that contain AE1, RhCx, EPB41, GYPC, XK, KEL and likely GLUT3 (Bennett, 1983; Reid *et al.*, 1990; Marfatia *et al.*, 1994; Nicolas *et al.*, 2003; Salomao *et al.*, 2008; Suzuki *et al.*, 2014). Other than GYPA which is an important part of the ankyrin complex, in this study glycophorin C (GYPC) is the only other detected murine glycophorin, important in maintaining RBC shape and deformability (Reid *et al.*, 1987), and comprises another ~5% of all PMA protein content (Table 7). GYPC is an important component of the protein 4.1 complex.

The transport activities of both ankyrin and 4.1 complexes are also likely modulated by interaction with STOM. STOM (#15 in rank abundance of PMA proteins but only 1.5% of RBC PMA protein proteome; Table 7) upregulates AE1 transporter activity (Genetet *et al.*, 2017) indirectly interacts with AQP1 in a cholesterol dependent manor, and probably also modulates P_{M,CO_2} via UT-B (Rungaldier *et al.*, 2013; Geyer *et al.*, 2013).

Other potential gas channels in the RBC membrane.

Because the double knockout (dKO) reduces P_{M,O_2} by ~55%, and pCMBS+dKO, reduces P_{M,O_2} by ~91% (paper #1), we consider which proteins or protein combinations in the murine RBC proteome could underlie the unassigned 36% of P_{M,O_2}. Below we consider membrane proteins with

permanent pores, or substrate translocation pathways, that even if O_2 does not permeate via their canonical transmembrane pathway, could open up transient O_2-permable "cracks" in the membrane as they cycle through their conformational changes.

Other aquaporins AQP1 is the only AQP detected in mouse RBCs in this study, and although human RBCs express the aquaglyceroporin AQP3 at ~30-fold lower levels than AQP1 (Roudier *et al.*, 1998) our findings align with previous reports that AQP3 is not functionally important in mouse RBC water or glycerol permeability (Yang *et al.*, 2001) and therefore no other AQP contributes to murine RBC P_{M,O_2}.

Solute transporters Table 8 lists the rank order of the SLC transporters detected in the RBC ghosts. AE1 is by far the most abundant species comprising ~20% of the PMA protein, As AE1 mediates the "chloride shift" in regions of higher metabolic activity (Hamasaki, 1999; Westen & Prange, 2003), acidifying the RBC lumen by exchanging intracellular HCO_3^- for extracellular Cl^- to facilitate O_2-release from Hb, the elevator mechanism that allows the AE1 protomers to alternate between open-to-out and open-to-in conformations may also open up non-canonical hydrophobic pathways in the transport and scaffold domains of each AE1 protomer (Huynh *et al.*, 2018; Zhekova *et al.*, 2022). Future physiology experiments and molecular dynamic simulation are required to determine whether AE1 mediates some or all of the remaining P_{M,O_2} present in dKO RBCs.

Altogether, the remainder of the solute transporters in Table 8 comprise ~5% of the PMA RBC protein which is an equivalent abundance to the Rh_{Cx} proteins. Like AE1, these species will transport their canonical substrates via elevator or "alternating access" mechanisms, and during this activity, transient O_2-permable pathways may open between the helices of the core and gate, or transport and scaffold domains in the SLC protomers.

Even though expressed below our AQP1-KO derived threshold for consequence for modulation of k_{HbO2}, the inferred abundance of the amino acid transporter heavy chain, SLC3A2 (CD98; PMA protein rank #123) significantly increases >60% in both AQP1-KO and dKO vs. WT samples (Figure 12N), while the abundance of the SLC7A5 large neutral amino acids transporter light chain (LAT1; PMA protein rank #140) with which SLC3A2 heterodimerizes similarly increases >60% in both AQP1-KO and dKO vs. WT samples (Supporting file 1). However, the differences in SLC7A5 abundance are not statistically significant (Statistics Table 2). Neither SLC3A2 nor SLC7A5 expression is altered vs. WT in RhAG-KO samples. SLC3A2 heterodimerization with SLC7A5 is a perquisite for plasma membrane expression (Cormerais et al., 2016; Ohgaki et al., 2017), but SLC3A2/SLC7A5 oligomers are characteristically absent from mature RBCs. Nonetheless, the SLC3A2/SLC7A5 heteroligomers are important during reticulocyte maturation and determining the eventual size and MHC of mature RBCs (Bouthelier et al., 2023). Our IFC data show that the reticulocyte and nucleated cell percentages in our samples are not significantly different (Table 2), suggesting that any observed knockout-dependent differences are likely attributable to variations in SLC3A2/SLC7A5 expression in AQP1-KO and dKO reticulocytes and/or erythroblasts present in the ghost samples rather than variation in their expression in mature RBCs. However, as we do not observe any significant effects on morphology or hematology in mature AQP1-KO and dKO RBCs, any SLC3A2/SLC7A5 mediated effects in the progenitor cells appear to be of little potential consequence for P_{M,O_2}.

The abundance of the H^+-coupled Zn^{2+} antiporter SLC30A1 (ZnT1; PMA protein rank #172)–also detected in human RBCs (Pasini *et al.*, 2006)–is 69% greater in the RhAG-KO and 46% greater in dKO vs. WT ghosts (Figure 12). Zinc transporter protein abundance in mature RBCs can be enriched by EPO in erythroid precursors prior to the terminal maturation in RBCs and in murine RBCs, and ZnT1 expression is reduced following dietary Zn^{2+} depletion (Ryu *et al.*, 2008). In the absence of such a crucial component of the erythrocyte membrane as RhAG in RhAG-KO and dKO RBCs, enhanced ZnT1 expression before RBC maturation could promote

Zn^{2+} uptake and stabilize RhAG-KO and dKO RBC membranes (Zheng *et al.*, 2023) making their morphology appear normal while missing a major constituent on the ankyrin and protein 4.1 complexes.

Ion channels The PIEZO1 stretch activated cation channel (Coste *et al.*, 2010; Gnanasambandam *et al.*, 2015; Fang *et al.*, 2021) is not tethered to the cytoskeleton and its distribution in the RBC surface is governed by membrane curvature and tension, tending to cluster within the concave dimple at the center of RBCs (Vaisey *et al.*, 2022). and it is involved in RBC sickling (Chow *et al.*, 2021). Missense mutations in *Piezo1* define the Er-blood group (Karamatic Crew *et al.*, 2023). Because PIEZO1 is adapted to gate cations, and is expressed in low abundance relative to other transporters at the RBC plasma membrane, it is an unlikely candidate to directly mediate substantial RBC gas exchange. However its ion channel activity, and surface distribution is of possible significance in modulating the permeability of other gas channel pathways identified in this study. The Ca^{2+} fluxes mediated by PIEZO1 in RBCs predominantly initiate various second messenger signaling pathways. One of the principal pathways entails the activation of calmodulin to regulate cytoskeletal protein interactions in complexes containing AE1, the Rh_{Cx} or AQP1, and facilitate the activation of numerous other signaling pathways (Takakuwa & Mohandas, 1988; Nunomura & Takakuwa, 2006; Nunomura *et al.*, 2011). Ca^{2+}- influx through PIEZO1 also modulates adenylyl cyclase activity. The resultant modulation in cAMP levels impacts protein kinase A (PKA) activity, resulting in additional downstream effects including but not limited to regulation of RBC volume, deformability, and aggregation (Muravyov & Tikhomirova, 2012).

Non-PMA proteins.

Determining the significance of any substantial difference in non-PMA proteins identified by LC/MS/MS is challenging, as we meticulously washed away the cytoplasmic contents from the RBC ghost samples. The proteins exhibiting substantial alterations constituted less than 0.1% of the overall ghost proteome, suggesting that the variances likely indicate minor sample-to-sample

variations in wash stringency during preparation rather than an important modulation in protein expression. Future investigations should investigate the modulation of expression of kinases, phosphatases and other enzymes that can potentially up- or downregulate functional expression of the principal proteins that mediate RBC P_{M,O_2}.

Conclusion

In mice genetically defective in *Aqp1* and/or *Rhag* only the targeted proteins are deleted and there are no other expression changes among the top 93% of plasma membrane associated proteins in expressed in murine RBCs. Furthermore, there are no substantial or significant differences in RBC morphology in AQP-1-KO, RhAG-KO or dKO. We quantify the increase in pCMBS- and DIDS- pretreatment poikilocytosis compared to non-treated cells and these parameters are then included in the linear combinations (step 14; Figure 13) to calculate shape-corrected k_{HbO2} (step 14; Figure 13; paper #1) which is then used to calculate shape corrected P_{M,O_2} (paper #3)

Acknowledgements

We thank Jean-Pierre Cartron for the gift of *Rhag*–/– mice, and for most helpful discussions. We thank Seong-Ki Lee for developing an improved approach for genotyping the *Rhag*–/– mice. We also thank Thomas Radford for organizing the husbandry of the mouse colonies; Gerald Babcock for his role as laboratory manager; Philip G. Woost of the CWRU Flow Cytometry and Imaging Microscopy Core (FCIMC) for his assistance with the flow cytometry data collection and analysis; Daniela Schlatzer of the CWRU Center for Proteomics and Bioinformatics for their assistance with mass spectrometry. This work was supported by Office of Naval Research (ONR) grant N00014-11-1-0889, N00014-14-1-0716, and N00014-15-1-2060; a Multidisciplinary University Research Initiative (MURI) grant N00014-16-1-2535 from the DoD, NIH grant multi-scale modeling grant 5U01GM111251 (to WFB), and NIH grant R01 HL160857 (to W.F.B.). W.F.B. gratefully acknowledges the support of the Myers/Scarpa endowed chair.

Tables

Table 1. Physiological solutions*

Component or parameter	Oxygenated solution (also, RBC washing)	De-oxygenated solution	Components for OOE Hemolysis assay			Solutions for preparation of mouse erythrocyte ghosts		
			A	B	Mix†	Sedimentation Buffer	Wash Buffer	Lysis Buffer‡
NaCl (mM)	92.5	15	140	116	128	150	150	0
KCl (mM)	0§	0§	3	3	3	0	0	0
$CaCl_2$ (mM)	0.01	0.01	2	0	1	0	0	0
Na_2HPO_4 / NaH_2PO_4 (mM)‖	44.9/13.1	44.9/13.1	0	0	0	4.06/0.94	0	0
HEPES (mM)	0	0	16	0	8	0	0	0
$NaHCO_3$ (mM)¶	0	0	~0	44	22	0	0	0
CO_2 (%)	0	0	~0	~1	0.5	0	0	0
pH	~7.40‖	~7.40‖	7.03#	8.41¶	~7.25	~7. 5‖	~7.0	~8.0
Pyranine (μM)Δ	0	0	0	2◊	1◊	0	0	0
RBCs or lysate	++	0	++▽	0	+▽	+	+	+
NDT♦	0	50	0	0		0	0	0
Tris-HCl (mM)	0	0	0	0	0	0	0	5
Dextran500(w/v)	0	0	0	0	0	0.75%	0	0
Temperature (°C)	RT	RT	10	10	10	RT	RT	RT
Osmolality (mOsm)	~300	~300	~295	~300	~298	_	~290	/

*This table shows the compositions of all the solutions used in either the present paper (1st in the series of 3) or the following paper (2nd of 3). The only solution in common with the two papers is the "Oxygenated solution". The "Deoxygenated solution" and the three "OOE" solutions ("A", "B", and "Mix") were used only in the present paper. The three "Solutions for the preparation of mouse erythrocyte ghosts" were used only in the following paper.

[†]The values in this "Mix" column are those at the instant of mixing solutions A and B (Zhao *et al.*, 2017). The solution is out of equilibrium because the pH of 7.25 is far too low for the system to be in equilibrium, given [HCO_3^-] = 22 mM and CO_2 = 0.5%. Note that both solutions "A" and "B" were equilibrated with room air and are thus oxygenated.

[‡]Complete protease inhibitor tablet (Roche) – only for lysis and first wash following lysis step.

[§](Coin & Olson, 1979) previously used 0 mM KCl in this solution.

[‖]The ratio [$HPO_4^=$]/[$H_2PO_4^-$] determines the pH at RT (~22°C).

[¶]The addition of HCO_3^- generates a trivial amount of CO_2 and also some $CO_3^=$, and spontaneously yields a pH of 8.41 at 10°C.

[#]We titrated HEPES free acid (pK ~7.41) to pH 7.03 with NaOH at 10°C.

[Δ][Pyranine] in the reaction cell was either 1 μM (to obtain pH data) or 0 μM (to obtain background data).

[◊]In the hemolysis assay, when determining the background for the fluorescence signal, we omitted the pyranine dye.

[▽]In the hemolysis assay, when determining the uncatalyzed rate constant (k_{uncat}) of the reaction $HCO_3^- + H^+ \rightarrow CO_2 + H_2O$, we omitted RBCs and lysate.

[♦]NDT is freshly added and used within ~1 hour. Final [NDT] in SF reaction cell is 25 mM.

Table 2. Percent mature vs. immature erythrocytes present in mouse blood, determined using IFC

Mouse	Mature RBCs		Reticulocytes		Nucleated cells	
	Mean	SD	Mean	SD	Mean	SD
WT	96.06	0.58	2.40	0.73	1.54	0.16
AQP1-KO	95.25	0.67	3.06	0.88	1.69	0.54
RhAG-KO	92.90	0.66	4.60	1.41	2.50	0.96
dKO	93.94	1.46	3.53	1.10	2.53	0.41

Each of the four data rows represents the average of four separate IFC runs on a single genotype. Mature RBCs constitute ≥93% of all cells in the blood samples acquired from WT, AQP1-KO, RhAG-KO, and double KO (dKO) mice. We performed a one-way ANOVA, followed by the Holm-Bonferroni correction (Holm, 1979; see Methods[37]), and observed no significant differences.

[37] See Methods>Flow cytometry (workflow #6 & #11)>Imaging flow cytometry (IFC)

Table 3. Quantification of major diameter ($Ø_{Major}$) by IFC, among various blood-cell types, from four mouse genotypes *

Mouse	Cell types	n total	Mean (μm)	SD	Mode (μm)	Median (μm)	IQR
WT	Mature RBCs	1156720	6.79	0.93	6.67	6.67	1.33
	Reticulocytes	29317	7.06	1.15	6.67	7.00	1.33
	Nucleated cells	18492	7.36	1.05	7.00	7.33	1.33
	All Immature cells	47809	7.18	1.12	7.00	7.00	1.33
	ALL CELL TYPES	1204530	6.80	0.94	6.67	6.67	1.33
AQP1-KO	Mature RBCs	1139890	6.68	0.90	6.67	6.67	1.33
	Reticulocytes	36806	6.77	1.15	6.67	6.67	1.33
	Nucleated cells	20044	7.14	1.01	7.00	7.00	1.00
	All Immature cells	56850	6.90	1.12	6.67	7.00	1.33
	ALL CELL TYPES	1196740	6.69	0.92	6.67	6.67	1.33
RhAG-KO	Mature RBCs	1077350	6.47	0.92	6.00	6.33	1.33
	Reticulocytes	53283	7.18	1.22	7.00	7.00	1.67
	Nucleated cells	29162	7.46	1.13	7.33	7.33	1.33
	All Immature cells	82445	7.28	1.20	7.33	7.33	1.33
	ALL CELL TYPES	1159800	6.53	0.97	6.00	6.33	1.00
dKO	Mature RBCs	1166840	6.52	0.92	6.33	6.33	1.00
	Reticulocytes	44110	6.94	1.21	6.67	7.00	1.67
	Nucleated cells	31462	7.32	1.04	7.33	7.33	1.33
	All Immature cells	75572	7.10	1.16	7.00	7.00	1.33
	ALL CELL TYPES	1242420	6.55	0.95	6.33	6.33	1.00

*Blood samples were taken from four age-matched mice of each genotype. The $Ø_{Major}$ of all RBCs and RBC precursor cells from blood of four strains of mice were analyzed after gating according to their fluorescence signature by IFC. One-way ANOVA with a Holm-Bonferroni means comparison (Holm, 1979) (see Methods) determined that differences between all pairs of mean $Ø_{Major}$ are statistically significant ($P<0.001$ for all comparisons).

Table 4. Summary of hematological data obtained from the subset of mice used in the IFC analysis and as basis for mathematical simulations*

Mouse	WT	Aqp1-KO	RhAG-KO	dKO
N	4	4	4	4
Age (weeks)	13.0 ±1.2	13.0 ±0.0	8.7 ±0.6	11.5 ±4.0
WBC (10^3/ul)	14.5 ±2.7	14.0 ±3.3	11.9 ±2.4	9.9 ±2.3
LYM (10^3/ul)	12 ±2.1	11.8 ±2.9	10.3 ±2.0	8.3 ±1.8
MONO (10^3/ul)	0.7 ±0.2	0.6 ±0.1	0.5 ±0.1	0.4 ±0.1
GRAN (10^3/ul)	1.9 ±0.9	1.7 ±0.3	1.2 ±0.4	1.3 ±0.5
LYM %	83.1 ±5.2	83.8 ±1.1	86.7 ±1.9	83.8 ±3.1
MONO %	4.0 ±0.8	3.7 ±0.5	3.3 ±0.4	3.6 ±1.0
GRAN %	12.9 ±4.4	12.5 ±1.1	10.0 ±1.5	12.7 ±2.5
HCT (%)	54.5 ±4.1	52.7 ±1.8	57.9 ±2.4	58.9 ±7.9
HGB (g/dl)	16.4 ±0.3	15.1 ±0.4 (†*P*=0.00316)	16.6 ±0.7	17.1 ±1.3
RDWa (fl)	32.9 ±1.7	34.5 ±1.1	36.6 ±0.9	36.4 ±3.2
RDW % (%)	17.3 ±0.5	17.5 ±0.4 (†*P*=0.00787)	17.9 ±0.3	18.4 ±0.5 (**P*=0.00311)
MCV (fl)	47.9 ±2.6	49.5 ±1.5	51.0 ±0.7	49.8 ±3.6
MCH (pg)	14.4 ±0.4	14.1 ±0.1	14.7 ±0.4	14.5 ±0.2
MCHC (g/dl)	30.1 ±2.1	28.6 ±0.6	28.7 ±0.4	29.4 ±2.4
RBC (10^6/μl)	11.4 ±0.4	10.6 ±0.3	11.3 ±0.5	11.8 ±1.0
PLT (10^3/μl)	286.3 ± 70.2	417.3 ± 59.6	467.8 ± 136.1	443.0 ± 150.0
MPV (fl)	6.5 ±0.4	6.5 ±0.3	6.5 ±0.4	6.2 ±0.1

*These data on 4×4 = 16 mice are a subset of the hematology data in #1>table 4. Each "N" represents an analysis of the blood from 1 mouse. We used these mice in the IFC studies (see Table 2 and Table 5) and as the basis for the mathematical simulations. Because we observed no statistically significant differences between sexes in #1>table 4 , we grouped a males and females for this study. dKO, double knockout (i.e.,

Aqp1–/–, *Rhag*–/–). We analyzed data using a one-way ANOVA, followed by the Holm-Bonferroni (Holm, 1979) correction (see Methods). For each parameter (e.g., MCV) we made all possible comparisons between from the four genotypes. * denotes a significant difference compared with WT. † denotes a significant difference compared with dKO. *P*-values are displayed in parentheses below the mean value if the comparison is significant.

Table 5. Quantification of $Ø_{Major}$, from IFC, among mature RBCs from WT and dKO mice treated with inhibitors *

Mouse	Drug	Cell shape	n total	%	$Ø_{Major}$ (μm)	SD	SEM
WT	No Drug	Biconcave Disk	224756	98.6	6.73	1.07	0.00225
		nBCD	3223	1.4	6.47	0.89	0.0157
	pCMBS	Biconcave Disk	111534	91.3	6.67	0.87	0.00183
		nBCD	10646	8.7	5.93	0.57	0.0101
	DIDS	Biconcave Disk	102170	59.0	6.43	0.79	0.0017
		nBCD	71075	41.0	5.77	0.70	0.0123
dKO	No Drug	Biconcave Disk	183684	97.5	6.22	0.82	0.00174
		nBCD	4726	2.5	6.11	0.57	0.00996
	pCMBS	Biconcave Disk	151278	94.3	6.59	0.92	0.00193
		nBCD	9184	5.7	5.90	0.59	0.0103
	DIDS	Biconcave Disk	141579	78.7	6.47	0.87	0.00184
		nBCD	38259	21.3	5.85	0.59	0.0104

* We split blood samples from three age-matched pairs of WT and dKO mice into three equal parts and incubated each of these with a different inhibitor (see Methods). We sorted RBCs according to their fluorescence signature by IFC and analyzed the number and $Ø_{Major}$ of normal RBCs and nBCD following each drug treatment (see Figure 7). dKO, double knockout (i.e., *Aqp1*–/–, *Rhag*–/–).

Table 6. Summary of automated hematological data obtained from the same samples used for IFC and for mathematical simulations

Mouse	WT			dKO		
N	3			3		
Age (weeks)	11.0 ±0.0			10.3 ±0.6		
groups	Ctrl	pCMBS	DIDS	Ctrl	pCMBS	DIDS
WBC (10^3/ul)	6.1 ±5.3	2.1 ±0.6	6.8 ±7.6	4.2 ±1.9	2.1 ±1.5	4.9 ±3.1
LYM (10^3/ul)	4.8 ±4.3	1.4 ±0.4	5.6 ±6.5	2.6 ±1.1	1.3 ±1.2	3.2 ±2.6
MONO (10^3/ul)	0.4 ±0.3	0.2 ±0.1	0.4 ±0.3	0.2 ±0.0	0.2 ±0.2	0.2 ±0.2
GRAN (10^3/ul)	0.9 ±0.7	0.5 ±0.2	0.8 ±0.8	1.4 ±1.6	0.6 ±0.2	1.5 ±1.5
LYM %	77.8 ±3.1	67.4 ±5.3*	77.3 ±10.4	66.9 ±21.1	55.8 ±20.2*	66.8 ±22.1
MONO %	4.6 ±2.0	8.9 ±2.5*	3.9 ±0.5	3.1 ±0.3	6.6 ±2.1*	4.1 ±1.0
GRAN %	17.6 ±4.7	23.6 ±2.8	18.8 ±10.6	30.0 ±12.3	37.6 ±22.2*	29.0 ±21.5
HCT (%)	35.5 ±5.5	36.1 ±5.2	36.5 ±3.3	33.9 ±2.8	38.7 ±4.8	35.7 ±2.9
HGB (g/dl)	11.3 ±0.9	11.9 ±0.9	11.5 ±0.5	10.3 ±0.7	12.2 ±1.2	11.3 ±1.3
RDWa (fl)	29.7 ±3.0	27.9 ±2.5*	31.1 ±2.6*	32.1 ±1.5	31.4 ±2.9*	34.1 ±2.0
RDW % (%)	16.9 ±0.4	17.1 ±0.9	17.2 ±0.2	16.5 ±0.5	16.9 ±0.6	17.1 ±1.1
MCV (fl)	46.0 ±3.9	44.2 ±3.6*	47.2 ±3.0	49.7 ±0.8	48.1 ±1.9*	50.7 ±0.4
MCH (pg)	14.7 ±0.2	14.8 ±0.2	14.9 ±0.4	15.1 ±0.1	15.1 ±0.2	16.0* ±0.6
MCHC (g/dl)	32.1 ±3.0	33.5 ±2.5*	31.6 ±2.0	30.5 ±0.5	31.5 ±1.0*	31.6 ±1.0
RBC (10^6/ul)	7.7 ±0.7	8.1 ±0.5	7.7 ±0.4	6.8 ±0.5	8.0 ±0.8	7.1 ±0.5
PLT (10^3/ul)	198.3 ±145.0	89.0 ±23.1	201.0 ±220.0	138.0 ±84.5	64.3 ±6.4	174.7 ±33.5
MPV (fl)	5.7 ±0.2	5.8 ±0.3	6.0 ±0.4	5.8 ±0.2	6.4 ±0.8	7.5 ±0.9

*These data on 3×2 = 6 mice are a subset of the hematology data in #1>table 5. We used these mice in the imaging–flow-cytometry studies on RBCs treated with inhibitors (see Figure 7 and as the basis for the mathematical simulations. Because we observed no statistically significant differences between sexes in #1>table 5, we grouped males and females (same gender for one pair of WT and dKO mice on that day) for

this study. dKO, double knockout (i.e., *Aqp1*–/–*Rhag*–/–). Results are presented as means ± SD. Each "N" represents an analysis of the blood from 1 mouse. Samples are tested at ostensibly 50% hematocrit (See Paper #1>Methods/Automated hematological analyses). We analyzed data using a one-way ANOVA, followed by the Holm-Bonferroni (Holm, 1979) correction (see Methods). For each parameter (e.g., MCV) from either WT or dKO, we made all possible comparisons between Ctrl, pCMBS and DIDS treatment. No significant differences were measured.

Table 7: Rank order in abundance, Protein IDs and Entrez Gene names for the 47 "Plasma-membrane–associated" (PMA) proteins with the largest inferred abundance in samples of RBC ghosts from WT mice

Rank order in abundance of all proteins	Rank order in abundance of PMA proteins[Δ]	Protein ID	% Total Proteome Abundance	% Total PMA Proteome Abundance	Entrez Gene Name
1	1	AE1*♥	9.45	19.55	solute carrier family 4 (anion exchanger), member 1 (Diego blood group)
2	2	GYPA*♥	8.99	18.61	glycophorin A
4	3	AQP1*♥	3.99	8.25	aquaporin 1 (Colton blood group)
8	4	GYPC*	2.64	5.47	glycophorin C (Gerbich blood group)
9	5	ANK1♥	2.05	4.25	ankyrin 1, erythrocytic (cytoskeletal protein)
12	6	SPTB♥	1.80	3.73	spectrin β, erythrocytic (cytoskeletal protein)
14	7	RhAG*♥	1.56	3.23	Rh-associated glycoprotein
15	8	EPB41	1.48	3.05	erythrocyte membrane protein band 4.1 (cytoskeletal protein)
16	9	EPB42♥	1.44	2.97	erythrocyte membrane protein band 4.2 (cytoskeletal protein)
17	10	MPP1	1.28	2.66	membrane protein, palmitoylated 1, 55 kDa (membrane-associated protein)
21	11	BSG*	1.03	2.13	basigin (CD147; Ok blood group)
23	12	SLC16A1*	0.90	1.86	solute carrier family 16 (monocarboxylate transporter), member 1 (MCT1)
24	13	RhD*♥	0.86	1.77	Rh blood group, CE/D homolog
25	14	CD47*	0.78	1.60	CD47 molecule
26	15	STOM*	0.74	1.52	Stomatin
28	16	DMTN	0.67	1.38	dematin actin binding protein (cytoskeletal protein)
33	17	SLC43A1*	0.47	0.96	solute carrier family 43 (amino acid system L transporter), member 1
36	18	CD36†	0.42	0.87	CD36 molecule (thrombospondin receptor)
37	19	SLC14A1*	0.38	0.79	solute carrier family 14 (urea transporter), member 1 (Kidd blood group) (UT1)
38	20	CLDN13*	0.38	0.79	claudin 13
42	21	TPM1	0.33	0.69	tropomyosin 1, alpha (cytoskeletal protein)
50	22	SLC16A10*	0.22	0.45	solute carrier family 16 (aromatic amino acid transporter), member 10
54	23	KEL*	0.20	0.41	Kell blood group, metallo-endopeptidase (membrane-associated protein)
57	24	CD59A	0.18	0.38	CD59A antigen (GPI-anchored membrane-associated protein)
59	25	RAC1	0.17	0.35	ras-related C3 botulinum toxin substrate 1 (membrane-associated protein)

61	**26**	**RAB8A**	**0.16**	**0.33**	RAB8A, member RAS oncogene family (membrane-associated protein)
65	**27**	**PLPP1***	**0.14**	**0.30**	Phosphatidic acid phosphatase type 2A
66	**28**	**GNA12**	**0.14**	**0.29**	G protein α12 (membrane-associated protein)
74	**29**	**SLC29A1***	**0.13**	**0.26**	solute carrier family 29 (equilibrative nucleoside transporter), member 1 (Ent1)
75	**30**	**HRAS**	**0.13**	**0.26**	Harvey rat sarcoma virus oncogene, GTPase (membrane-associated protein)
83	**31**	**TSPAN33***	**0.11**	**0.23**	tetraspanin 33
86	**32**	**ABCG2**	**0.11**	**0.23**	ATP-binding cassette transporter, sub-family G, member 2 (J.R. blood group)
89	**33**	**ATP2B2***	**0.10**	**0.22**	ATPase, Ca^{2+} transporting, plasma membrane 2
93	**34**	**STXBP5**	**0.10**	**0.20**	syntaxin binding protein 5 (tomosyn)
95	**35**	**TSPAN8***	**0.10**	**0.20**	tetraspanin 8
97	**36**	**GP1BB†**	**0.09**	**0.20**	glycoprotein Ib (platelet), β polypeptide
98	**37**	**VIPAS39**	**0.09**	**0.20**	VPS33B interacting protein, apical-basolateral polarity regulator, spe-39 homolog
99	**38**	**CRIP2**	**0.09**	**0.19**	cysteine rich protein 2
104	**39**	**XK***	**0.09**	**0.19**	X-linked Kx blood group
108	**40**	**SLC29A2***	**0.09**	**0.18**	solute carrier family 29 (equilibrative nucleoside transporter), member 2 (Ent2)
117	**41**	**ATP1B2**	**0.08**	**0.17**	ATPase, Na^+/K^+ transporting, β2 polypeptide
120	**42**	**VAMP3***	**0.08**	**0.16**	vesicle-associated membrane protein 3
123	**43**	**GP9†**	**0.08**	**0.16**	glycoprotein IX (platelet)
124	**44**	**NPTN***	**0.08**	**0.16**	neuroplastin
125	**45**	**GNAI2**	**0.08**	**0.16**	G protein α–inhibiting activity polypeptide 2
127	**46**	**CR1L***	**0.08**	**0.16**	complement component (3b/4b) receptor 1-like
134	**47**	**DNAJC5**	**0.07**	**0.15**	DnaJ (Hsp40) homolog, subfamily C, member 5

[Δ]Plasma-membrane–associated proteins (PMA Proteins).

*Integral membrane protein, known to be present in erythrocytes.

†Integral membrane protein, known to be present in platelets

‡ Membrane-associated protein, known to be present in white cells

♥ A component of the ankyrin complex

Table 8: Rank order in abundance of plasma-membrane–associated SLC proteins in WT RBC ghosts

Rank order Proteins		Primary accession	Protein ID	Alt. Protein ID	RBC Proteome		Full Protein name	Mean Intensity (AUC)	St. Dev	n
All	PMA$^{\Delta}$				% Total	%PMA				
1	1	P04919	SLC4A1	AE1	9.45	19.6	Anion exchange protein 1	2.61×10^{9}	4.91×10^{9}	171
23	12	P53986	SLC16A1	MCT1	0.898	1.86	Monocarboxylate transporter 1	2.48×10^{8}	2.38×10^{8}	27
33	17	Q8BSM7	SLC43A1	LAT3	0.466	0.964	Large neutral amino acids transporter small subunit 3	1.29×10^{8}	1.90×10^{8}	42
37	19	Q8VHL0	SLC14A1	UT-B	0.384	0.795	Urea transporter 1	1.06×10^{8}	8.62×10^{7}	36
50	22	Q3U9N9	SLC16A10	MCT10	0.218	0.451	Monocarboxylate transporter 10	6.02×10^{7}	5.86×10^{7}	30
74	29	Q9JIM1	SLC29A1	ENT1	0.127	0.263	Equilibrative nucleoside transporter 1	3.50×10^{7}	4.26×10^{7}	33
108	40	Q61672	SLC29A2	ENT2	0.0892	0.185	Equilibrative nucleoside transporter 2	2.46×10^{7}	4.57×10^{5}	3
142	51	Q9JHI9	SLC40A1	MTP1	0.0707	0.146	Ferroportin	1.95×10^{7}	1.10×10^{7}	24
180	65	O88343	SLC4A4	NBCe1	0.0573	0.119	Electrogenic Na^{+} HCO_3^{-} cotransporter 1	1.58×10^{7}	3.39×10^{6}	3
215	74	P32037	SLC2A3	GLUT3	0.0432	0.0893	Facilitated glucose transporter member 3	1.19×10^{7}	1.09×10^{7}	21
349	93	Q61165	SLC9A1	NHE1	0.0268	0.0555	Na^{+}/H^{+} exchanger 1	7.41×10^{6}	4.18×10^{6}	24
350	94	P58735	SLC26A1	SAT1	0.0268	0.0554	Sulfate anion transporter 1	7.40×10^{6}	3.41×10^{6}	6
490	123	P10852	SLC3A2*	MDU1	0.0171	0.0355	Amino acid transporter (CD98 Antigen)	4.73×10^{6}	2.28×10^{6}	30
533	132	P49282	SLC11A2	DMT1	0.0154	0.0318	Natural resistance-associated macrophage protein 2	4.24×10^{6}	2.99×10^{6}	12
555	134	Q09143	SLC7A1	CAT1	0.0146	0.0302	High affinity cationic amino acid transporter 1	4.03×10^{6}	4.92×10^{5}	3
594	140	Q9Z127	SLC7A5	LAT1	0.0133	0.0276	Large neutral amino acids transporter small subunit	3.68×10^{6}	2.76×10^{6}	12
669	151	Q60857	SLC6A4	SERT	0.0116	0.0240	Na^{+}-dependent serotonin transporter	3.20×10^{6}	2.98×10^{6}	3
729	161	P28571	SLC6A9	GLYT1	0.0101	0.0208	Na^{+} Cl^{-}-dependent glycine transporter 1	2.78×10^{6}	1.91×10^{6}	6
737	164	Q6X893	SLC44A1	CD92	0.00987	0.0204	Choline transporter-like protein 1	2.73×10^{6}	1.01×10^{6}	9
793	173	Q60738	SLC30A1*	ZnT1	0.00875	0.0181	H^{+}-coupled Zn^{2+} antiporter	2.42×10^{6}	7.40×10^{5}	12
850	181	Q9WVC8	SLC26A3	DRA	0.00741	0.0153	Cl^{-} anion exchanger	2.05×10^{6}	4.61×10^{5}	3

917	**191**	**Q3UHH2**	**SLC22A23**	**OCT2**	**0.00605**	**0.0125**	Organic cation transporter 2	1.67×10^{6}	1.66×10^{5}	3
940	**193**	**P41438**	**SLC19A1**	**RFC1**	**0.00558**	**0.01154**	Reduced folate transporter	1.54×10^{6}	2.00×10^{5}	3
1092	**210**	**Q8BRU6**	**SLC18A2**	**VAT2**	**0.00149**	**0.00307**	Synaptic vesicular amine transporter	4.10×10^{5}	2.15×10^{5}	3

Plasma-membrane–associated proteins (PMA proteins). n is the number of total peptides detected for each protein from 3 individual mouse samples (i.e. number of unique peptides for each protein =n/3). * indicates that this protein exhibits a significant difference in its inferred abundance in one or more of the KO mouse strains (Figure 12). Gray shaded rows have an abundance ≤ that for detected AQP1 peptides in the AQP1-KO and dKO ghosts.

Table 9: Rank order in abundance, Protein IDs and Entrez Gene of all non-membrane-associated proteins with significant changes in abundance in RBC ghosts from one or more of the KO or dKO mice strains as detailed in Figure 12

Rank order in abundance of all proteins	Protein ID	% Total proteome abundance	Entrez Gene Name
101	**PSMA4**	**0.0917**	proteasome (prosome, macropain) subunit, alpha type, 4
130	**C17ORF99**	**0.0755**	chromosome 17 open reading frame 99 (Protein IL-40)
132	**FLNA**	**0.0753**	filamin A, alpha (cytoskeletal protein)
133	**PSMA1**	**0.0745**	proteasome (prosome, macropain) subunit, alpha type, 1
195	**MYH9**	**0.0501**	myosin, heavy chain 9, non-muscle (cytoskeletal protein)
214	**DHTKD1**	**0.0433**	dehydrogenase E1 and transketolase domain containing 1 (mitochondrion)
236	**CAPN5**	**0.0395**	calpain 5 (Protease)
433	**ATP2A3**	**0.0203**	ATPase, Ca^{++}-transporting, ubiquitous (a SERCA)
448	**CAPN1**	**0.0194**	calpain 1 (protease)
1045	**MUG1**	**0.00353**	murinoglobulin 1 (proteinase)
1051	**ALDH18A1**	**0.00337**	aldehyde dehydrogenase 18 family, member A1
1052	**MMP21**	**0.00322**	matrix metallopeptidase 21
1059	**RPL8**	**0.00291**	ribosomal protein L18
1087	**RNF213**	**0.00158**	ring finger protein 213
1095	**NDUFA12**	**0.00128**	NADH dehydrogenase (ubiquinone) 1 alpha subcomplex, 12
1102	**SNX12**	**0.000604**	sorting nexin 12

Table 10: Rank order in abundance, Protein IDs and Entrez Gene of all PMA proteins with significant changes in abundance in RBCs from one or more of the KO or dKO mice strains as detailed in Figure 12.

Rank order in abundance of all proteins	Rank order in abundance of PMA proteins[Δ]	Protein ID	% Total Proteome Abundance	%PMA Proteome Abundance	Entrez Gene Name
136	48	ITGA2B†	0.0726	0.150	integrin, α2b (platelet glycoprotein IIb of IIb/IIIa complex, antigen Cd41)
138	49	NRAS	0.0723	0.150	neuroblastoma RAS viral (v-ras) oncogene homolog (GTPase)
177	63	ADAM10‡	0.0579	0.120	ADAM metallopeptidase domain 10 (peptidase)
469	118	TBXAS1†	0.0179	0.0370	thromboxane A synthase 1 (platelet)
490	123	SLC3A2♦	0.0171	0.0355	solute carrier family 3 (amino acid transporter heavy chain), member 2
655	144	ICAM4*	0.0118	0.0244	intercellular adhesion molecule 4 (Landsteiner-Wiener blood group)
793	172	SLC30A1*	0.00875	0.0181	solute carrier family 30 (zinc transporter), member 1
952	194	H2-D1‡	0.00538	0.0111	major histocompatibility complex
1066	206	CAPRIN1‡	0.00244	0.00510	cell cycle associated protein 1
1069	208	DLG1‡	0.00241	0.00500	discs, large homolog 1 (Drosophila)
1100	212	TMEM106B‡	0.000773	0.00160	transmembrane protein 106B (lysosome)

[Δ]Plasma-membrane–associated proteins (PMA proteins).

*Integral membrane protein, known to be present in erythrocytes.

♦Integral membrane protein, known to be present in erythroblasts.

†Integral membrane protein, known to be present in platelets.

‡ Membrane-associated protein, known to be present in white cells.

Gray shaded rows have an abundance ≤ that for detected AQP1 peptides in the AQP1-KO and dKO ghosts.

Figure Legends

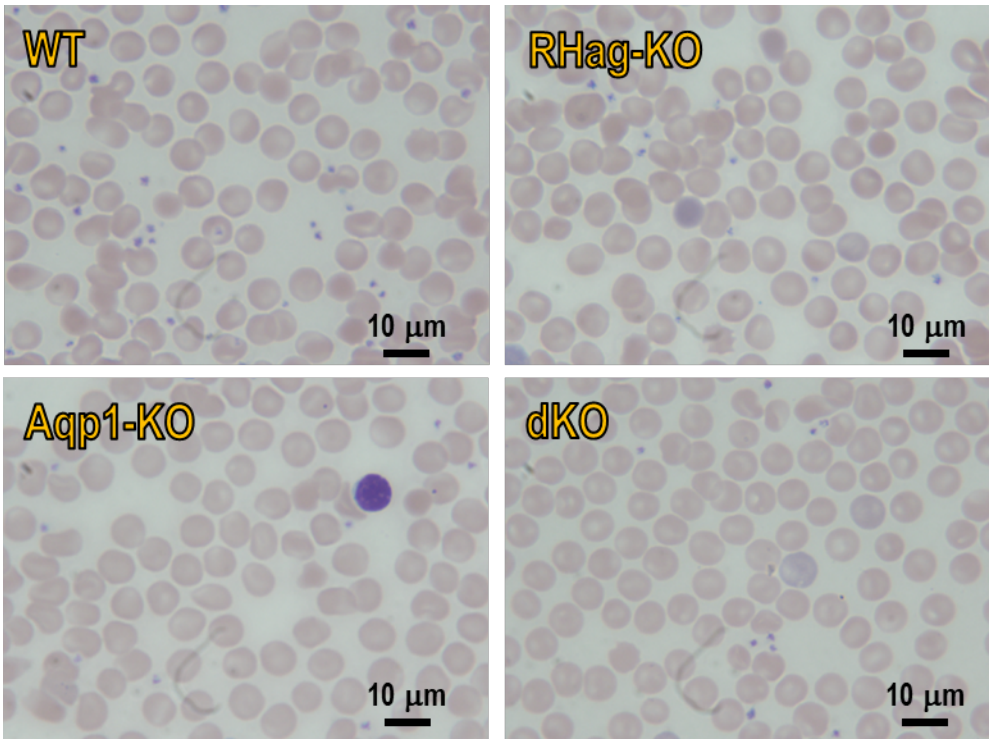

Figure 1. Representative blood smears from each of four genotypes

We generated 12 Wright-Giemsa stained air-dried peripheral blood smears from WT, AQP1-KO, RhAG-KO and dKO mice (i.e., 4 smears from each of 3 separate mice), for a total of 48 smears. No differences in red cell morphology are noted among knockout strains and WT mice. Photos are taken at 1000× magnification.

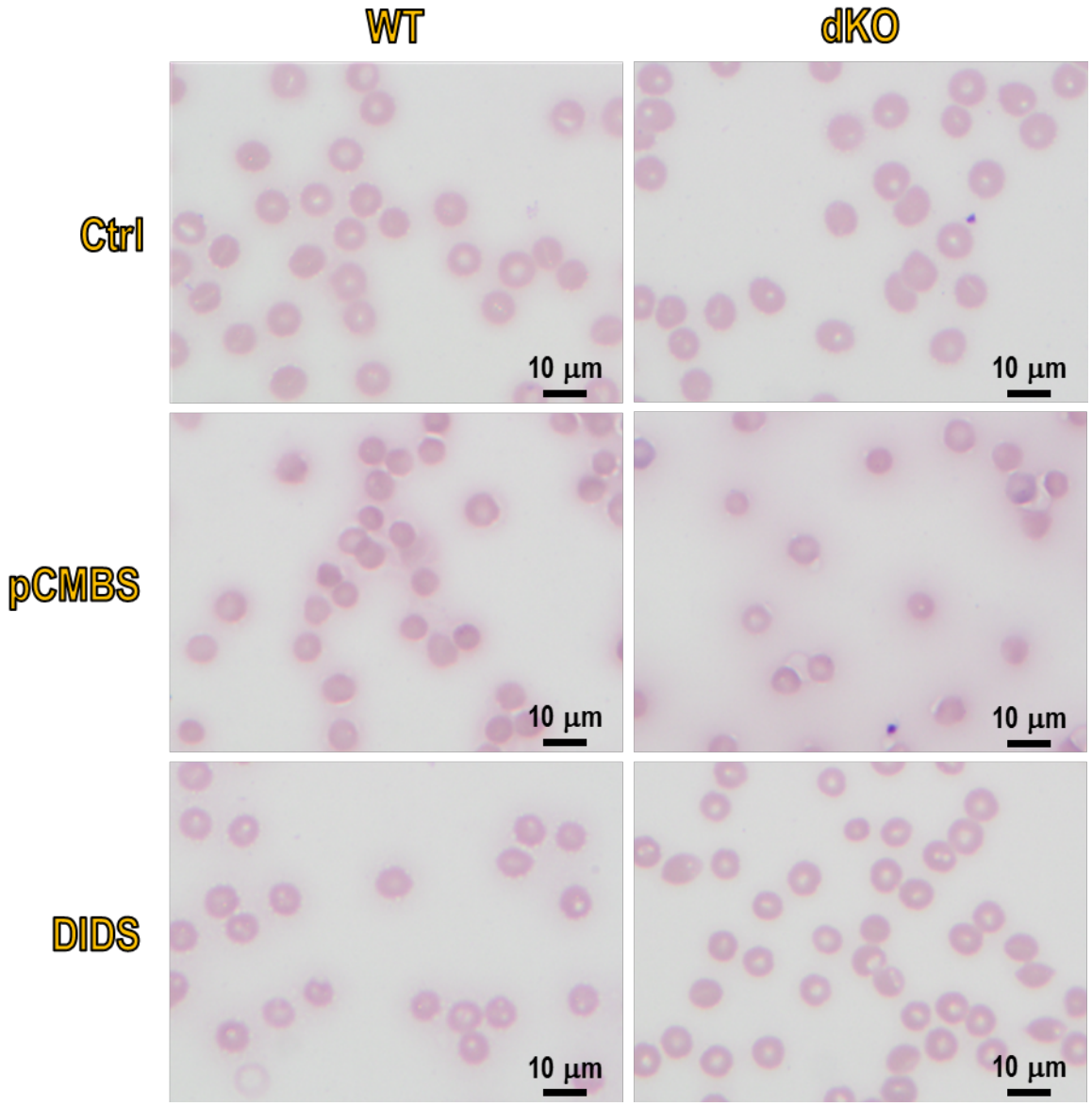

Figure 2. Representative blood smears from WT and dKO mice, of cells treated with inhibitors

Representative images (1000× magnification) of Wright-Giemsa stained air-dried peripheral blood smears using blood obtained from WT mice (left column row) and dKO mice (right column), either in control conditions (Ctrl; top row) or with a 15 min pretreatment with 1 mM pCMBS (middle row) or a 1 h pretreatment with 200 μM DIDS (bottom row). No significant differences in red cell morphology were noted between WT and dKO mice under any tested conditions.

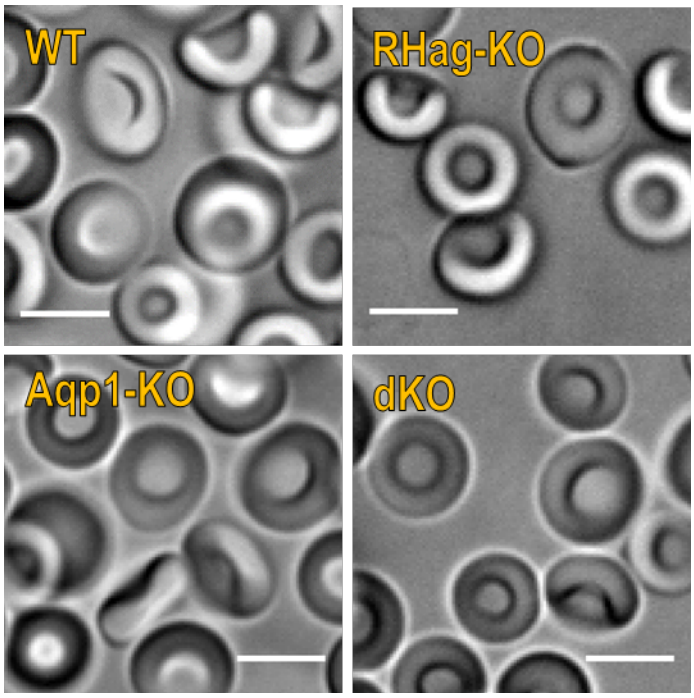

Figure 3. Representative DIC still micrographs of living RBCs

DIC micrographs of fresh RBCs from WT and the three KO mouse strains (annotated in the top left corner of each panel), tumbling through plane of focus and revealing normal biconcave disks. On a given day, we reviewed 4 to 5 samples (i.e., droplets) of RBCs suspended in oxygenated solution for 1 mouse of each genotype. We executed this protocol on 3 separate days, for a total of 3 separate mice/genotype (i.e., a total of 12 to 15 samples/genotype). Red cell morphology is similar in all groups and is unremarkable, with no differences noted among knockout strains and WT mice. The bar represents 5 μm. See (Supporting video 1, Supporting video 2, Supporting video 3, and Supporting video 4) for a representative DIC video clip of each genotype (i.e., WT, Aqp1-KO, RhAG-KO, dKO); each clip shows RBCs tumbling through the plane of focus.

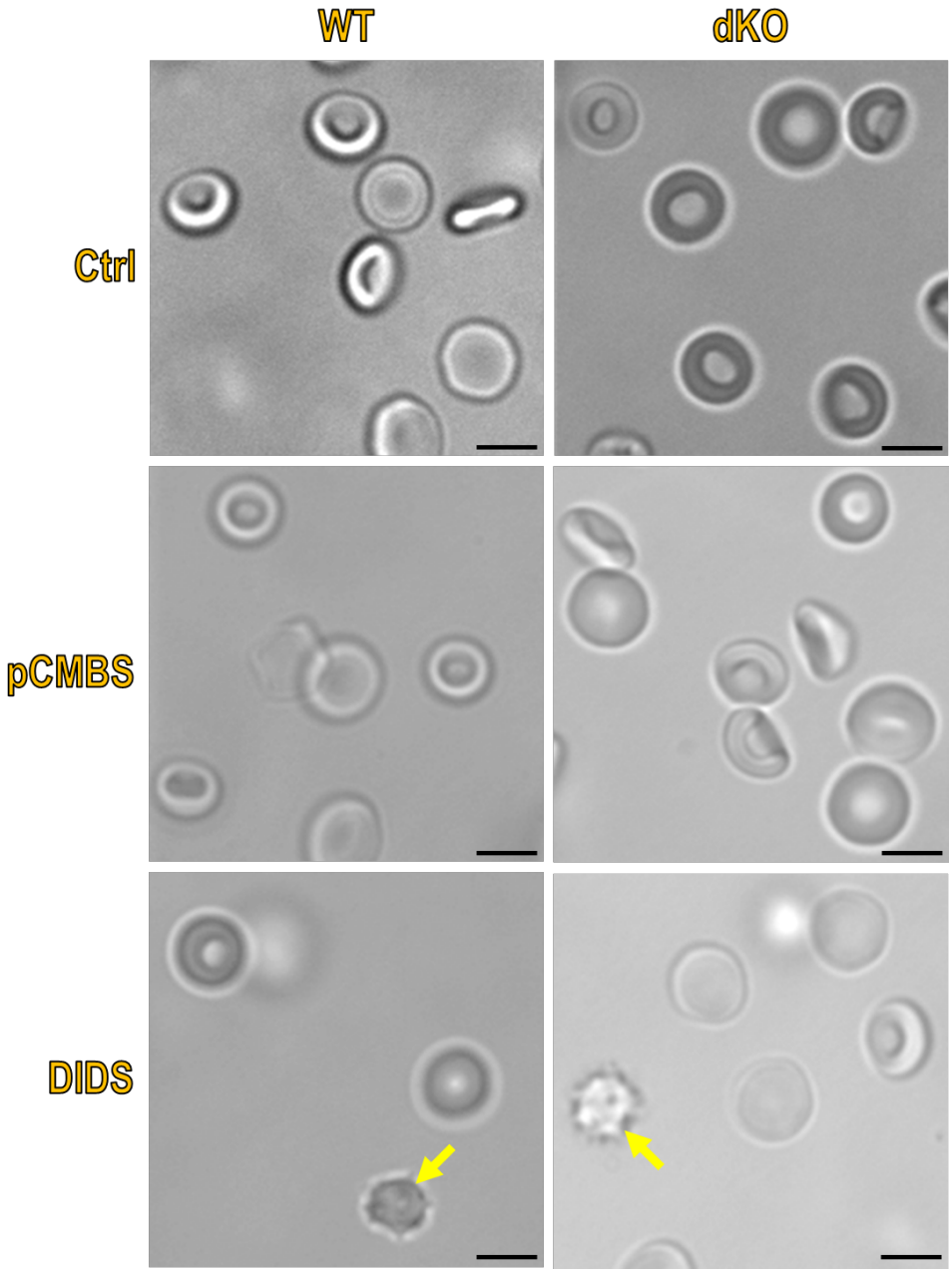

Figure 4. Representative DIC still micrographs of living RBCs, treated with inhibitors

On a given day, we reviewed 4 to 5 samples (i.e., droplets) of RBCs suspended in oxygenated solution for 1 mouse of each of genotype. We executed this protocol on 3 separate days, for a total of 3 separate mice/genotype (i.e., a total of 12 to 15 samples/genotype). Red cell morphology is similar in control groups and is unremarkable, with no differences noted among dKO and WT mice. For both WT and dKO mice, treatment of RBCs with inhibitors tended to cause the appearance of small, spherical cells with spicules (yellow arrows), more so in DIDS-treated than in pCMBS-treated cells. We can also identify these tumbling spherocytes by microvideography (not shown). The scale bar represents 5 μm.

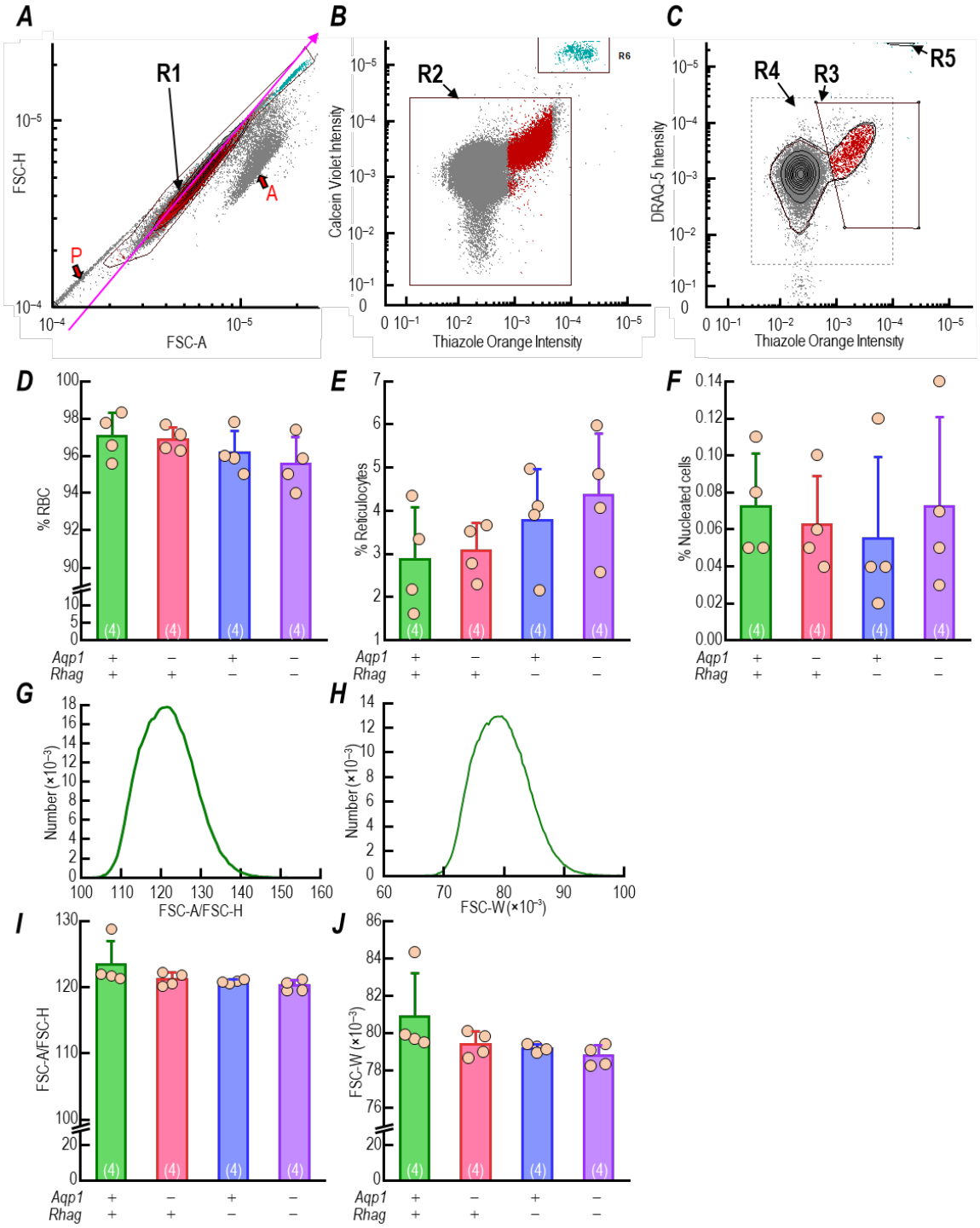

Figure 5. Light-scattering flow cytometry

We sort mature RBCs from their precursors in the LSRII device in order to perform size and shape analyses.

In panels A-C and G and H we display representative data from one WT sample.

A, Singlet cells in the R1 region of the FSC-A/FSC-H plot are individual viable blood cells. An arrow pointing from the red letter "P" annotates the gray coordinates representing small particulates and the arrow pointing from the red letter "A" annotates coordinates for cell aggregates. The red and dark-cyan colored pixels represent reticulocytes (identified by the R3 region, panel *C*) and nucleated cells (identified by the R5 region, panel *B & C*) respectively, and the coloring is applied using Boolean logic) after the regions in panels *B* and *C* are applied.

B, The cells within R1 from panel *A* are plotted in a TO vs. CV intensity plot confirming that all are intact and alive. Two distinct clusters are observed and are set as the regions R2 and R5. R5 included cells with high TO and CV intensity are also observed in Panel *C* and classified there.

C, When analyzing the R1 cells on a TO vs. DRAQ-5 intensity plot we see the R5 cluster also has the highest TO^+ and DRAQ-5^+ signals. These are the CV^+ nucleated cells that are colored dark-cyan in Panels *A-C*. A region (R3) isolates reticulocytes (red pixels) within R4. The R4 contour captures 99% of the enucleated cells, representing the erthrocytic populations (RBCs and reticulocytes). Cells in panel *B* were already gated in panel *A* (i.e., they are all single cells). The mature RBCs are both TO^- and DRAQ-5^-. Reticulocytes (red points) are TO^+ but DRAQ-5^{dim}. Nucleated cells are the brightest TO^+ and DRAQ-5^+ cells. .

D, Summary of the mean %RBCs from 4 samples each of WT, AQP1-KO, RhAG-KO and dKO blood. The break in the y-axis is from 12-89%.

E, Summary of the mean %reticulocytes from 4 samples each of WT, AQP1-KO, RhAG-KO and dKO blood.

F, Summary of the mean %nucleated cells from 4 samples each of WT, AQP1-KO, RhAG-KO and dKO blood.

In Panels *D-F*, mouse genotype is indicated by a + or – for *Aqp1* and *Rhag* below each of the columns, which are colored green for WT, pink for AQP1-KO, blue for RhAG-KO and purple for dKO. Individual data points from each sample are plotted on top of the columns and error bars represent SD. We measure no significant differences between all possible comparisons by performing a one-way ANOVA, followed by the Holm-Bonferroni correction (see Methods).

G, Representative RBC-only Boolean-gated single parameter frequency distribution of forward-scatter intensity area (FSC-A)/forward scatter pulse height (FSC-H; see Methods from the WT sample in panel *A* (This plot is the equivalent of traveling up the (magenta) diagonal arrow of the FSC-H v FSC-A plot in panel *A* with the nucleated cells (R5) and reticulocytes (R3) excluded.

H, Representative RBC-only Boolean-gated single parameter frequency distribution of forward-scatter intensity width (FSC-W; see Methods) from the WT sample in panel *A*.

I, Summary of the mean FSC-A/FSC-H ratio from 4 samples each of WT, AQP1-KO, RhAG-KO and dKO blood. Individual data points from each sample are plotted on the bars. The break in the y-axis is from 28-99.

I, Summary of the mean FSC-W value from 4 samples each of WT, AQP1-KO, RhAG-KO and dKO blood. The break in the y-axis data is between 28×10^{-3} to 75×10^{-3}.

In Panels *G-I*, genotypes and columns are annotated and colored as in panels *D-E.* Individual data points from each sample are plotted on top of the columns and error bars represent SD. We measure no significant differences between all possible comparisons by performing a one-way ANOVA, followed by the Holm-Bonferroni correction (see Methods). CV, calcein violet (viability); TO, thiazole orange (RNA); and DRAQ-5, Deep Red Anthraquinone 5 (DNA).

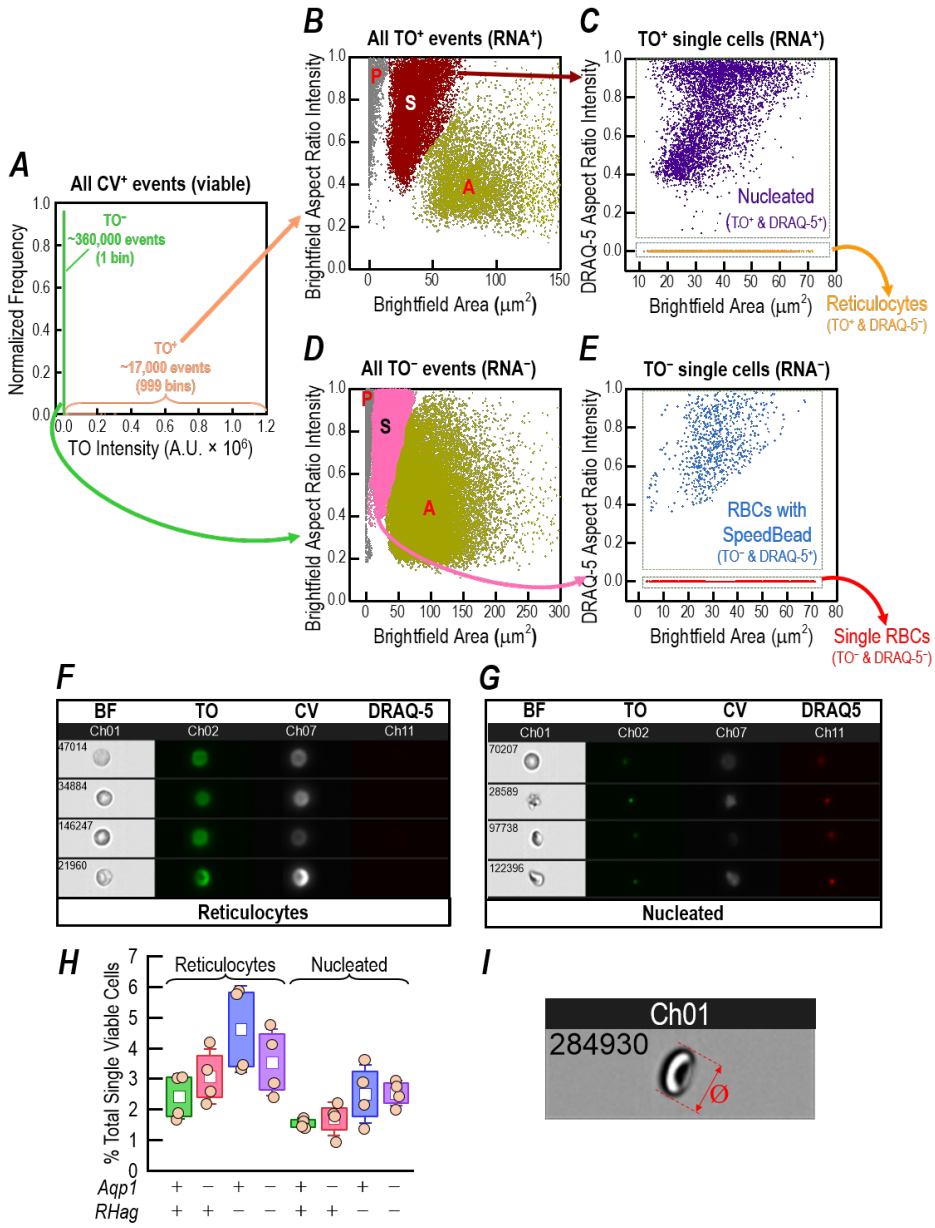

Figure 6. Imaging flow cytometry (IFC)

IFC gating schemes established to allow analysis of individual mature RBCs and other non-mature RBC types. We sort mature RBCs from their precursors and nucleated cells by IFC in order to perform further size and shape analyses. We begin in panel *A,* with all CV-positive cells (CV⁺) and within this population distinguish TO⁺ (peach) from TO⁻ cells (green). In panel *B*, which plots the brightfield area vs. the brightfield aspect ratio of the TO⁺ cells sorted from panel *A,* we isolate the single TO⁺ cells (S; burgundy data points) from small particles (P; gray data points) or aggregated cells (A; drab-olive data points). In panel *C,* plots of the brightfield area vs. DRAQ-5 aspect ratio intensity for the single TO⁺ cell population from panel *B*, further isolates the nucleated TO⁺ and DRAQ-5⁺ cells (purple data points) from reticulocytes (TO⁺ DRAQ-5⁻; orange

data points). In panel *D*, which plots the brightfield area vs. the brightfield aspect ratio of the TO^- cells sorted from panel *A,* we isolate the single TO^+ cells (S; pink data points) from small particles (P; gray data points) or aggregated cells (A; drab-olive data points). In panel *E,* plots of the brightfield area vs. DRAQ-5 aspect ratio intensity for the single TO^- cell population from panel *D*, further isolates the TO and DRAQ-5^+ population that represents RBCs with a contaminating speed bead in the same image (blue data points) from single mature RBCs (TO and DRAQ-5^-; red data points). Panel *F* displays example images of cells classified as reticulocytes according their CV^+, TO^+ and DRAQ-5^- fluorescent signature. Panel *G* displays example images of cells classified as nucleated according their CV^+, TO^+ and DRAQ-5^+ fluorescent signature, which have a heterogeneous morphology. In both panels *F* and *G* the channels are assigned in order of increasing fluorescence excitation wavelength. *H,* Percent of total cell count represented by cells not defined as mature RBCs for each genotype, identified by TO and DRAQ-5 staining as in Panel *C*. Each mouse genotype is color-coded green (WT), pink (Aqp1-KO), blue (RhAG-KO), or purple (dKO). The presence of *Aqp*1 or the *RhAG* gene is annotated at the base of each box plot. The cell classification is annotated above the braces grouping each set of 4 box plots. The mean for each group is plotted as an open square, the boxes represent the interquartile range, and the whiskers represent SD. The four individual data points (beige circles) overlaying each box pot report the normalized % total cells represented by each cell classification in a single blood sample. One-way ANOVA, followed by the Holm-Bonferroni (Holm, 1979) correction (see #2>Methods/Statistical analysis) determines that there are no significant differences vs. WT. *I,* After gating in IFC according to their fluorescence signature (Panels *A*→*E*), the $Ø_{Major}$ of RBCs and non-RBCs were determined by measuring the length of the longest axis (red box) of the cells in the corresponding BF images. Every cell is annotated with a unique numeric identifier in the top left of the image. In *A*–*E*, CV, calcein violet (viability); TO, thiazole orange (RNA-stain); DRAQ-5, Deep Red Anthraquinone 5 (DNA-stain). BF, brightfield image.

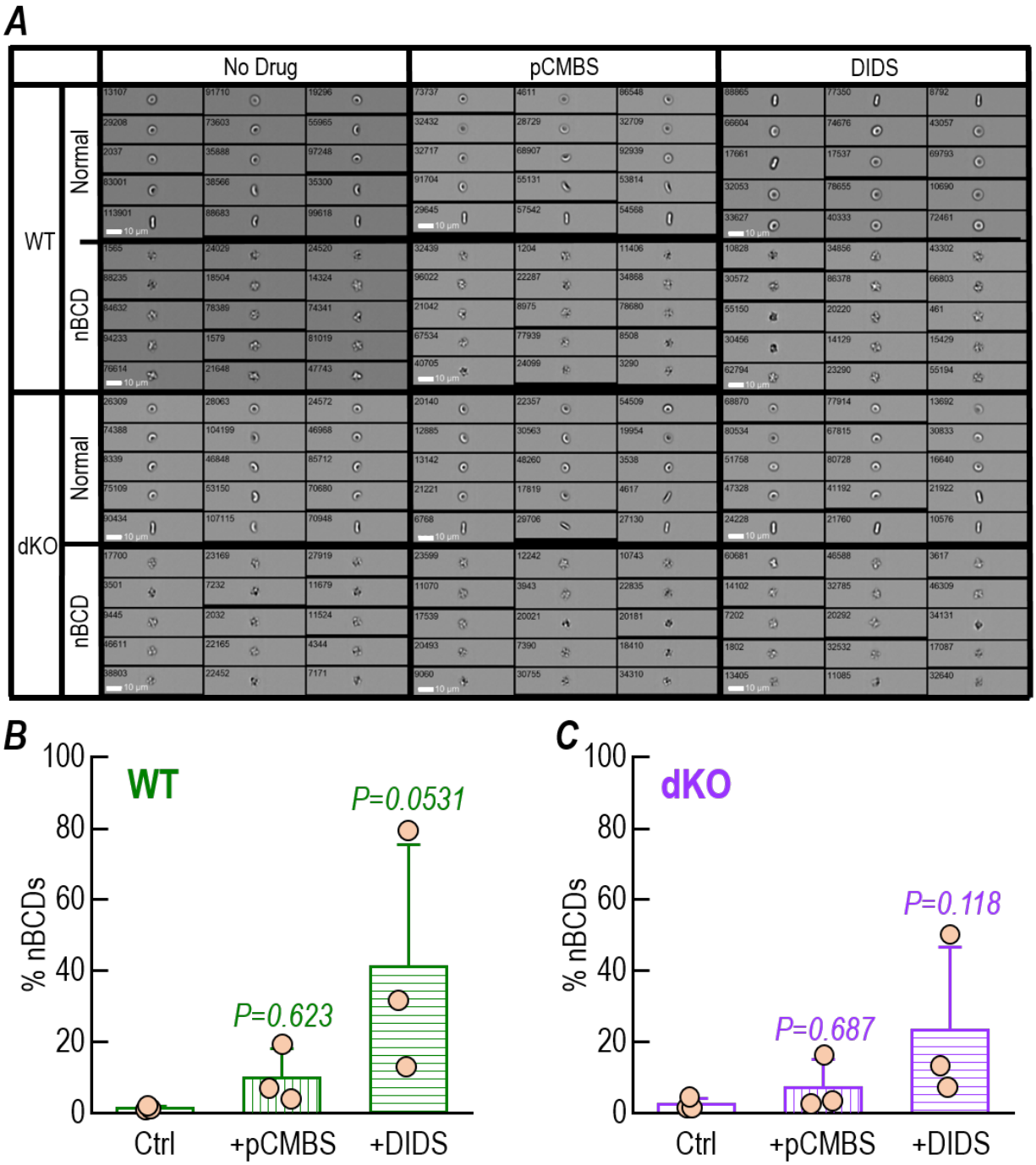

Figure 7. Analysis of bright-field images of WT or dKO RBCs from IFC quantify nBCD prevalence following incubation with no drug, pCMBS or DIDS

A, We collected blood samples and pre-incubated with no drug (Ctrl), 1 mM pCMBS for 15 min, or 200 μM DIDS for 1 h as described in Methods. For Ctrl, 1 mM pCMBS and 200 μM DIDS drug-treatment conditions

we show 15 examples of normal biconcave disc shaped RBCs or non-biconcave disc (nBCD) shaped from WT and dKO blood. *B,* IFC analysis of the degree of non-BCD formation in experiments on WT RBCs treated with pCMBS or DIDS. *C,* Prevalence of nBCDs among RBCs, treated with pCMBS or DIDS, from dKO mice. In both panels *B* and *C* Bars represent means ± SD and we performed one-way ANOVA, followed by the Holm-Bonferroni correction (see Methods) to test for significant differences between Ctrl and the two drug-treated conditions on WT or dKO RBCs. *P*-values vs. Ctrl are reported above each drug-treated bar. Experiments were performed on blood samples from 3 age-matched pairs of WT vs dKO mice.

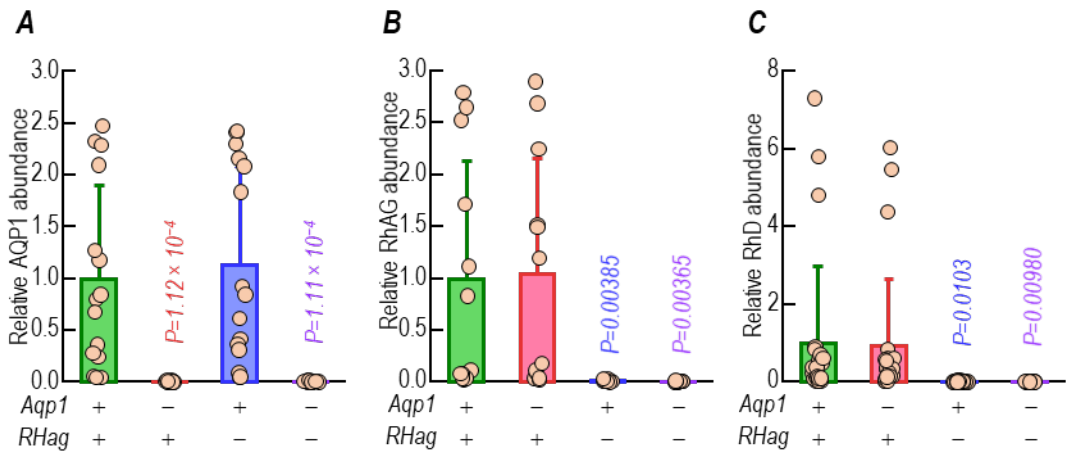

Figure 8. Effect of genetic deletions of *Aqp1*, *Rhag*, or both on AQP1, RhAG and RhD protein expression.

Proteomic analysis by LC/MS/MS of all peptides of *A*, AQP1, *B*, RhAG, and *C*, RhD from WT (green bars), AQP1-KO (pink bars), RhAG-KO (blue bars) or dKO (purple bars) RBC ghosts, normalized to 1 for WT. The x-axis annotation reports whether the *Aqp1* or *Rhag* genes are present (+) or not (−). Bars represent normalized mean peak intensity (AUC) ± SD. Each individual data point (beige circles) reports the normalized abundance of one unique peptide detected from one ghost sample purified from one mouse (e.g., in panel *A*, for AQP1 protein, we plot 15 individual data points overlaying each bar, representing 5 unique peptides, from 3 RBC ghost samples from each of four strains). We performed one-way ANOVA with the Holm-Bonferroni correction to test for statistical significance, as described in the Methods[38], *P*-values for significant differences versus WT in that panel abundance appear above the appropriate bars.

[38] See Methods>Statistical analysis

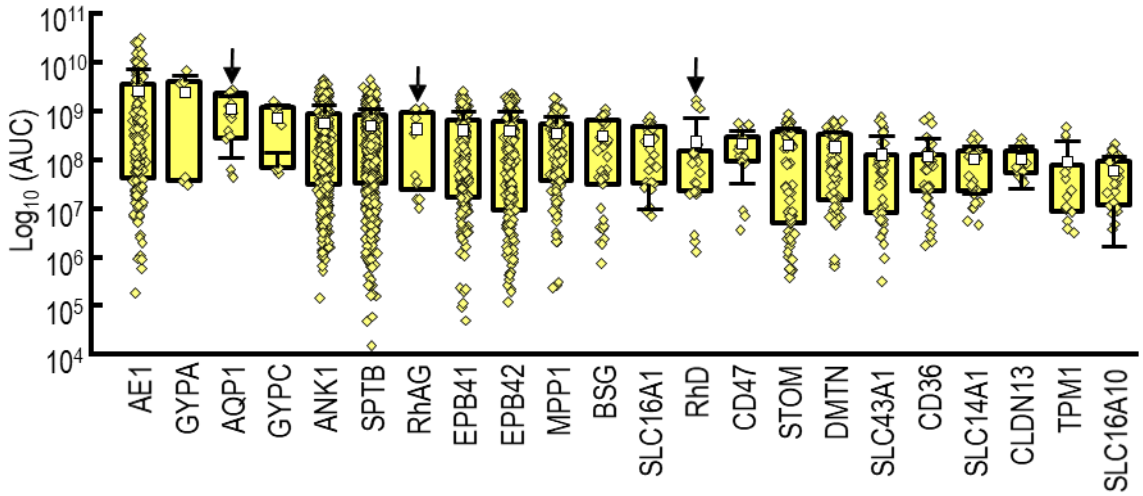

Figure 9. Proteomic analysis by LC/MS/MS of proteins in samples of RBC ghosts from WT mice

A, Plasma-membrane–associated proteins, ranked by abundance, as inferred from mass-spectrometry. AUC is area under curve. We detected a total of 7,188 unique peptides from 1,104 unique proteins, not all of RBC origin (Supporting file 1). Of these, 1,902 peptides and 212 proteins are "plasma-membrane–associated" (integral-membrane proteins + others) as defined by the data-analysis software Peaks (see Methods/Proteomic analysis). Each individual data point (yellow diamonds) overlaying a box plot reports the abundance of one unique peptide detected from one ghost sample purified from one mouse (e.g., for AE1 we plot 171 individual data points overlaying each bar, representing 57 unique peptides, from 3 RBC ghost samples from the WT mice). None of the 47 PMA proteins of greatest inferred abundance exhibited a significant change in response to any of the deletions. Of these 47, panel *A* shows the 22 PMA proteins, with greatest inferred abundance (Table 7 provides protein glossary and rank order of abundance of all 47 PMA proteins). Arrows Aqp1, RhAG, and RhD which are the targets of the genetic KO mice. Of these 22 most abundant PMA protein species, only the intended target proteins in each KO strain display a significant change in abundance. See Figure 9*A* and *B* for effects of gene deletions on abundance of Aqp1, RhAG, and RhD. See Figure 10, for effects of gene deletions on abundance of each of these 22 proteins. Others have shown that RhD expression requires *Rhag* in mice (Goossens *et al.*, 2010). Boxes represent the interquartile range. Open white squares represent the mean abundance. Whiskers represent one standard deviation. We performed one-way ANOVA with the Holm-Bonferroni correction to test for statistical significance, as described in Methods.

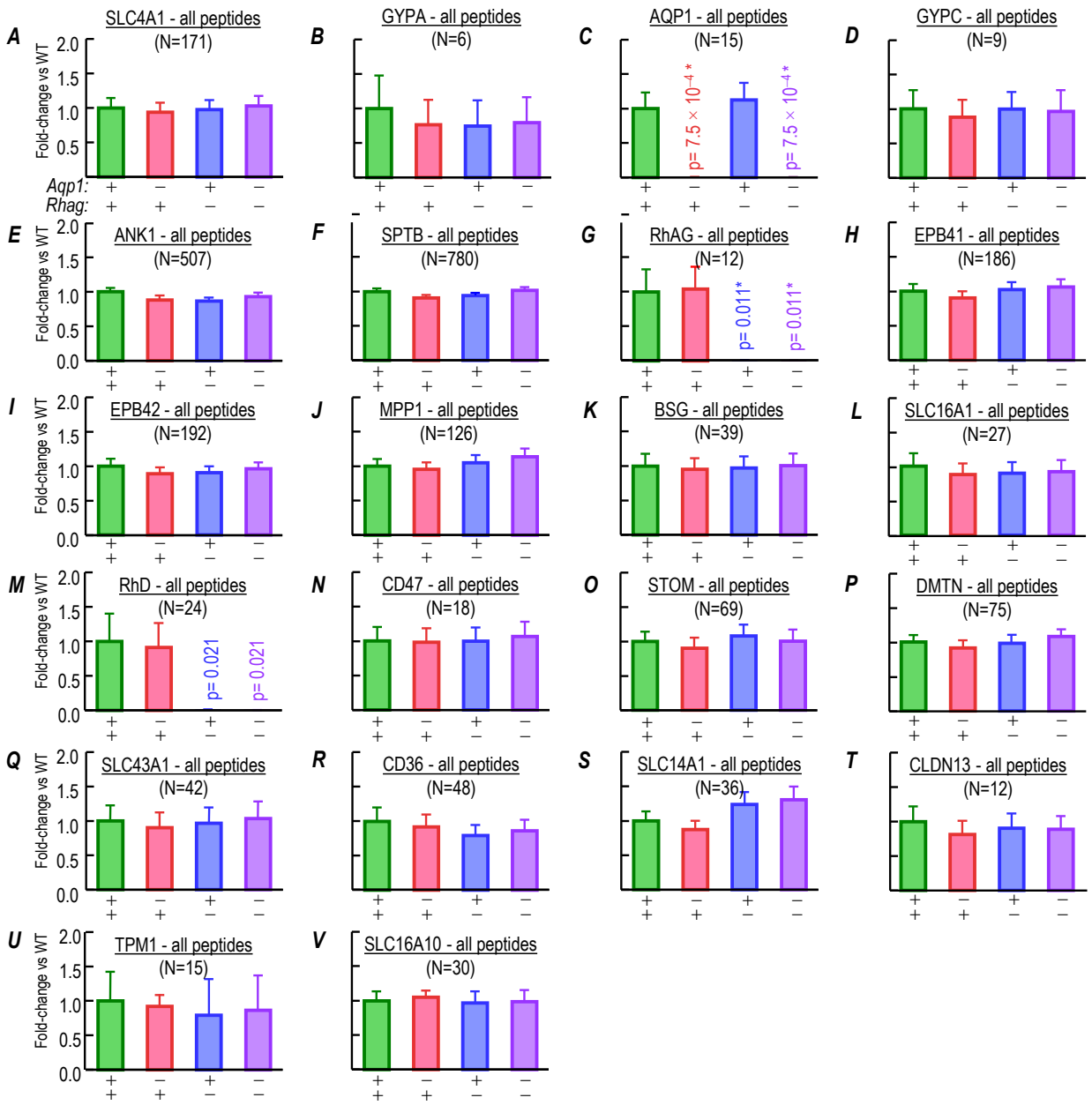

Figure 10. Summary of fold-changes in expression of 22 "plasma membrane – associated" proteins comparing samples from RBC ghosts of WT vs. AQP1-KO, RhAG-KO and double-KO (dKO) mice

These 22 panels represent the 22 plasma-membrane–associated proteins, from among the 50 proteins with the greatest inferred abundance in RBC ghosts from WT mice. The panels are in rank order, based on the inferred abundance of the protein in cells from WT mice (see Figure 9*A*). In each panel, data from WT mice (green bar) is the reference value for fold-changes in expression for the each mouse knockout strains (AQP1-KO, red bars; RhAG-KO, blue bars; dKO, purple bars), as determined by a mass-spectrometry based investigation of peptide peak intensity (AUC) obtained from RBC ghosts. We purify proteins from RBC ghosts of 3 mice/genotype (same samples as Figure 12) and the numbers in parentheses above the plot in each

panel are the total number of peptides analyzed for each protein from blood samples acquired the 3 mice per genotype (e.g. for AE1, peptide peak intensities are measured for 57 unique peptides from 3 mice for a total of n=171 replicates).

A, AE1 (SLC4A1).

B, glycophorin A (GYPA).

C, aquaporin 1 (AQP1).

D, glycophorin C (GYPC).

E, ankyrin 1 (ANK1).

F, erythrocytic spectrin beta (SPTB).

G, Rhesus blood group associated Glycoprotein A, RhAG (SLC42A1).

H erythrocyte membrane protein band 4.1 (EPB41).

I, erythrocyte membrane protein band 4.2 (EPB42).

J, membrane protein, palmitoylated 1 (MPP1).

K, basigin (BSG).

L, monocarboxylic acid transporter member 1, MCT-1 (SLC16A1).

M, mouse Rhesus blood group, D antigen (RhD).

N, CD47 molecule (CD47).

O, stomatin (STOM).

P, dematin actin binding protein (DMTN).

Q, solute carrier family 43 (amino acid system L transporter), member 1(SLC43A1).

R, CD36 antigen (CD36).

S, urea transporter member 1, UT-1 (SLC14A1).

T, claudin 13 (CLDN13).

U, tropomyosin 1 (TPM1).

V, monocarboxylate transporter member 10, MCT-10 (SLC16A10).

Bars represent the mean ± SD. peak intensity (AUC) for all peptides from each protein, normalized to the abundance in WT. Number of detected peptides per protein is displayed in parentheses. Not all of these proteins are necessarily RBC integral membrane proteins. We performed a one-way ANOVA, followed by the Holm-Bonferroni correction (Holm (1979); see Methods[39]). *P*-values vs. WT for the effect of genetic deletions of *Aqp1*, *Rhag*, or both on AQP1, RhAG and RhD protein expression are displayed above bars in panels *C* and *G*. The analyses show that expression of the target protein in RBCs of each knockout strain is essentially abolished. However, the difference in expression of other the RBC proteins in each knockout strain is not significant compared to WT. See Table 7 for glossary and rank order of abundance. See Supporting file 2 for *P*-values for all comparisons.

[39] See Methods>Statistical analysis

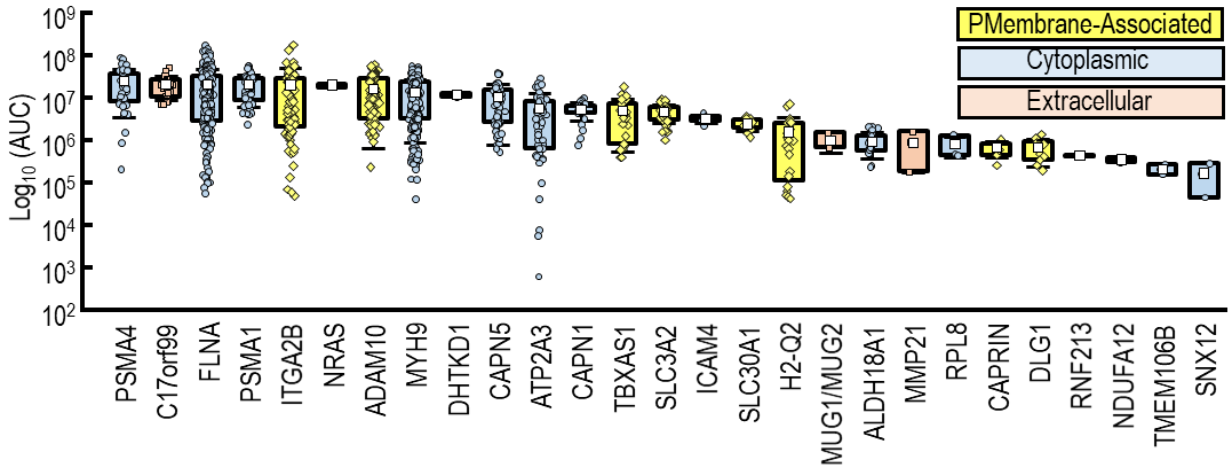

Figure 11. Proteomic analysis by LC/MS/MS of proteins in samples of RBC ghosts that demonstrate a significant difference from WT in one or more of the KO mouse strains

Ranking of the inferred abundance of the unique peptides from the 27 proteins (out of all 1,104 detected by mass spectrometry) from RBC ghosts that demonstrated a significant difference from WT in one or more of the KO mouse strains. Each individual data point (yellow diamonds, PMA-proteins; blue circles, cytoplasmic proteins; apricot squares, extracellular proteins) overlaying a box plot reports the abundance of one unique peptide detected from one ghost sample purified from one mouse (e.g., for Integrin α2b, Itga2b, we plot 81 individual data points overlaying each bar, representing 27 unique peptides, from 3 RBC ghost samples from the WT mice). For protein glossary and rank order by inferred abundance, see Table 9 for non PMA proteins and Table 10 for PMA. Figure 12 shows the effects of gene deletions on abundance of each of these 27 proteins. The colors of the panel backgrounds indicate the expected major location of each the proteins, as assigned by the data-analysis software Peaks (see Supporting file 1): yellow (plasma-membrane–associated), blue (cytoplasmic), and apricot (extracellular). For both panels *A* and *B*, we purified proteins from RBC ghosts of 3 mice/genotype. Each individual data point reports the abundance of one unique peptide detected from one ghost sample purified from one mouse (e.g., in Panel A, for RhAG protein, there are 12 individual data points, from 4 unique peptides, from 3 WT RBC ghost samples). Boxes represent the interquartile range. Open white squares represent the mean abundance. Whiskers represent one standard deviation. We performed one-way ANOVA with the Holm-Bonferroni correction to test for statistical significance, as described in Methods.

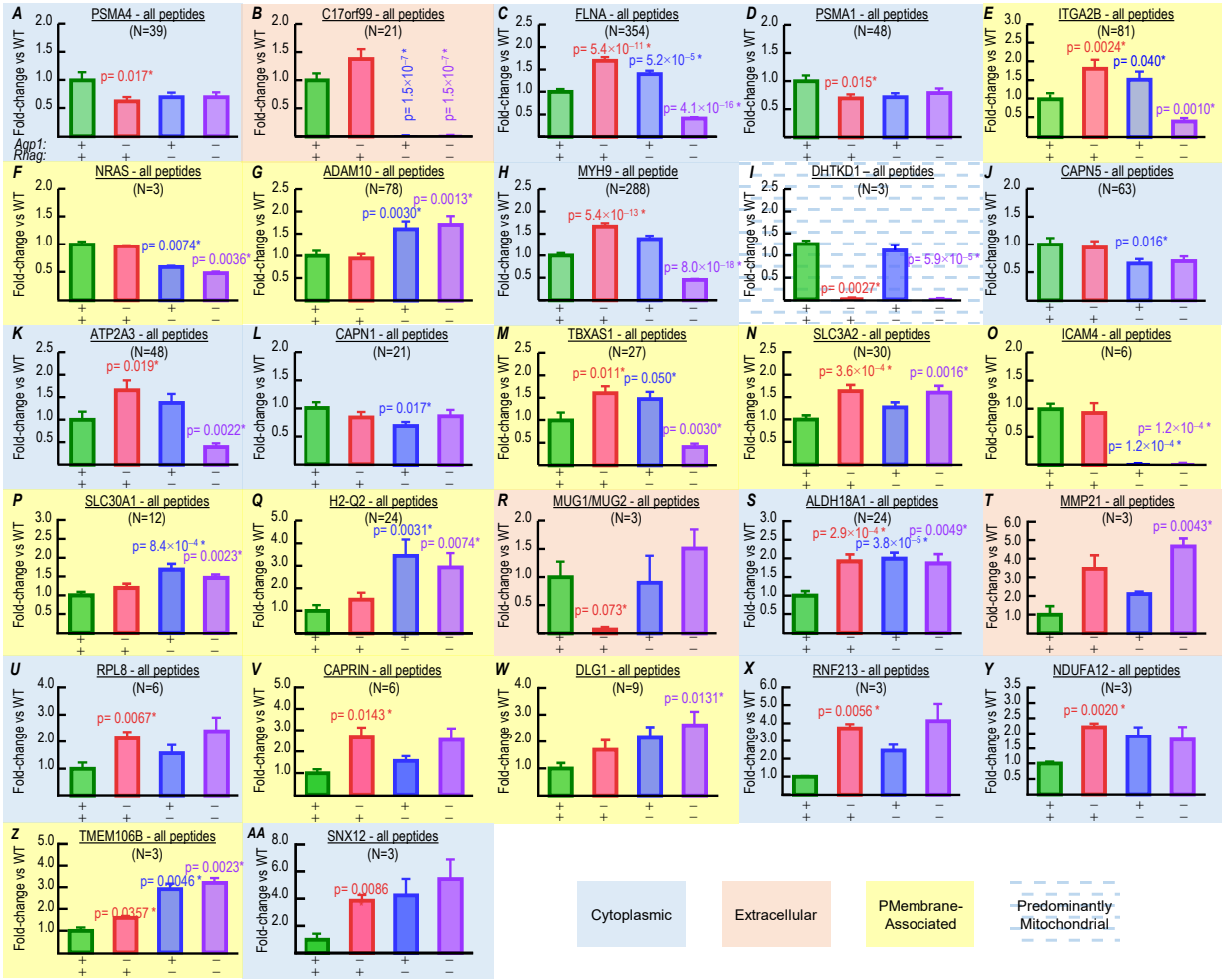

Figure 12. Summary of fold-changes in expression of all 27 proteins in which abundance changed in at least one KO genotype, comparing samples from RBC ghosts of WT vs. Aqp1-KO, RhAG-KO, and double-KO (dKO) mice

These 27 panels represent the 27 proteins—from among all 1105 detected proteins—that exhibited a significant change in at least one knockout strain vs. WT mice. The panels are in rank order, based on the inferred abundance of the protein in cells from WT mice (see Figure 9*B*). In each panel, data from WT mice (green bar) is the reference value for fold-changes in expression for the mouse knockout strains (Aqp1-KO, red bars; RhAG-KO, blue bars; dKO, purple bars), as determined by a mass-spectrometry based investigation of peptide peak intensity (AUC) obtained from RBC ghosts.

A, proteasome (prosome, macropain) subunit, alpha type, 4 (PMSA4).

B, Interleukin 40 (IL-40) from chromosome 17 open reading frame 99 (C17orf99).

C, filamin A, alpha (FLNA).

D, proteasome (prosome, macropain) subunit, alpha type, 1 (PSMA1).

E, integrin, alpha 2b (ITGA2B).

F, neuroblastoma RAS viral (v-ras) oncogene homolog (NRAS).

G, ADAM metallopeptidase domain 10 (ADAM10).

H, myosin, heavy chain 9, non-muscle (MYH9).

I, dehydrogenase E1 and transketolase domain containing 1 (DHTKD1).

J, calpain 5 (CAPN5).

K, ATPase, Ca^{++}-transporting, ubiquitous (ATP2A3).

L, calpain 1 (CAPN1).

M, thromboxane A synthase 1 (platelet) (TBXAS1).

N, solute carrier family 3 (amino acid transporter heavy chain), member 2 (SLC3A2).

O, intercellular adhesion molecule 4 (ICAM4).

P, solute carrier family 30 (zinc transporter), member 1, Zn-T1 (SLC30A1).

Q, major histocompatibility complex (H2-Q2).

R, Murinoglobulin 1 (MUG1/MUG2).

S, aldehyde dehydrogenase 18 family, member A1 (ALDH18A1).

T, matrix metallopeptidase 21 (MMP21).

U, ribosomal protein L8 (RPL8).

V, cell cycle associated protein 1 (CAPRIN1).

W, discs, large homolog 1 (Drosophila) (DLG1).

X, ring finger protein 213 (RNF213).

Y, NADH dehydrogenase (ubiquinone) 1 alpha subcomplex 12 (NDUFA12),

Z, transmembrane protein 106B (TMEM106B).

AA, sorting nexin 12 (SNX12).

Bars represent the mean ± SD peak intensity (AUC) for all peptides from each protein normalized to the

abundance in WT. Number of peptides per protein is displayed in parentheses. Not all of these proteins are from RBCs, let alone RBC integral membrane proteins. The colors of the bars indicate the location of the proteins, as assigned by the Peaks software: yellow (plasma-membrane associated), blue (cytoplasmic), and apricot (extracellular). We purified proteins from RBC ghosts of 3 mice/genotype (same samples as Figure 10). We performed a one-way ANOVA, followed by the Holm-Bonferroni correction (Holm (1979); see Methods). *Significant vs. WT. See Table 7*BC* for glossary.

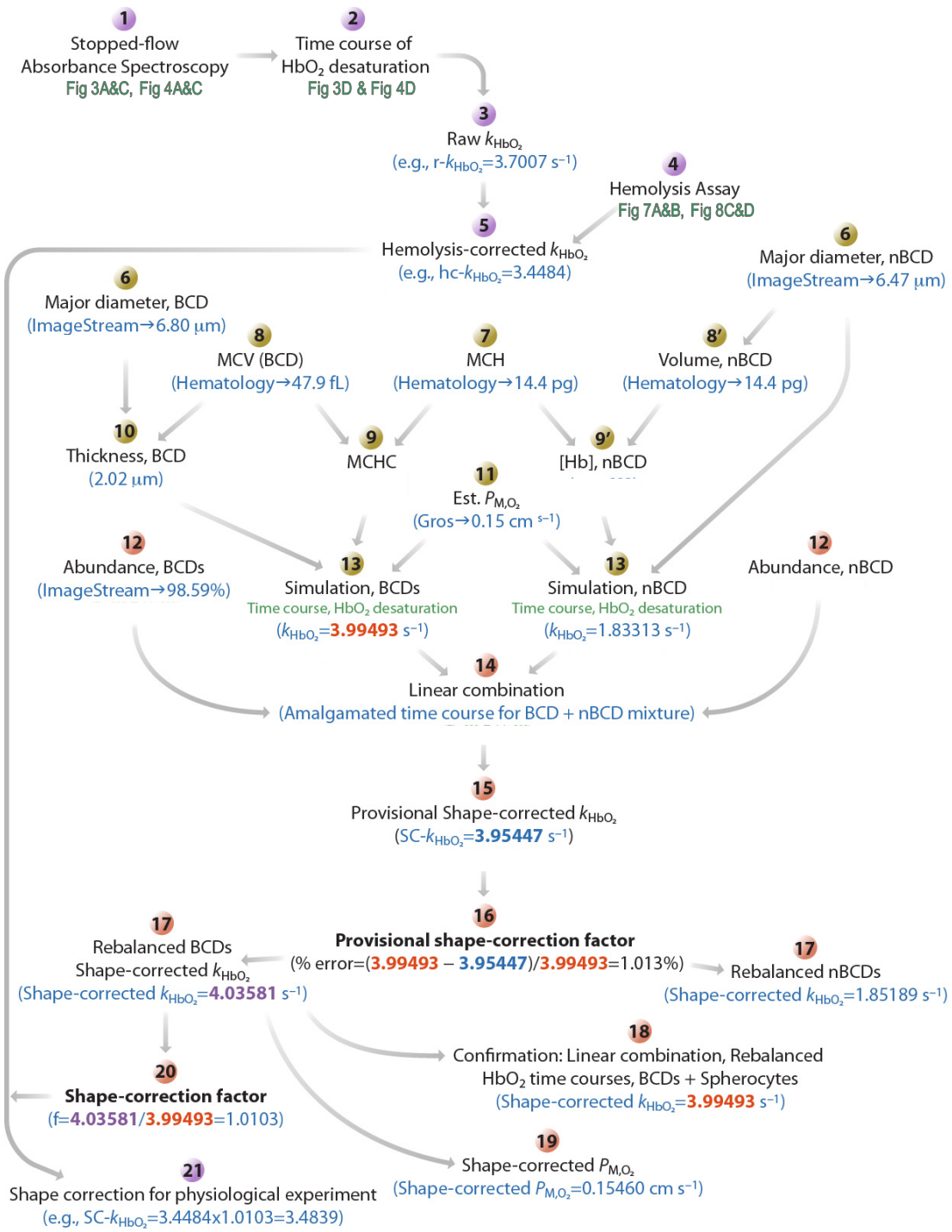

Figure 13. Workflow to obtain hemolysis-corrected and shape-corrected values of P_{M,O_2}

The numerals 1 through 21 indicate the steps summarized in the present paper—and detailed, as appropriate, in the present paper, paper #2, or paper #3—to arrive at first a hemolysis-corrected (HC) k_{HbO2}

and ultimately a shape-corrected (SC) k_{HbO_2}. At each step, we provide example values, if possible, and example figure in the present paper or paper #1 and paper #3.

We repeat workflow steps 1–5 for each experiment, ultimately arriving at a HC-k_{HbO_2} value for each. Step 6 applies to biconcave disks (BCDs), whereas step 6' applies to non-biconcave disks (nBCDs). The same is true for steps 8 and 8', 9 and 9', 12 and 12', 13 and 13', as well as for 17 and 17'. Hb, hemoglobin; k_{HbO_2}, rate constant for deoxygenation of intracellular HbO_2; MCH, mean corpuscular hemoglobin; MCHC, mean corpuscular hemoglobin concentration; MCV, mean corpuscular volume; P_{M,O_2}; membrane permeability to O_2.

.

Statistics Tables

Tables of *P*-values for one-way ANOVA with Holm-Bonferroni post-hoc means comparison for comparisons of differences in inferred abundance of the SLC transporter proteins listed in Table 8 between each of the three knockout mouse strains and WT. The table is split in two halves, with FWER set at 0.05, the upper half shows the adjusted α-value for each comparison and the lower half the *P*-value. Significant *P*-values are highlighted bold.

Statistics Table 1 Comparison of SLC3A2 (MDU1) inferred abundance

Mouse		WT	AQP1-KO	RhAG-KO	dKO
	P \ α		α	α	α
WT			0.00833	0.0250	0.0100
AQP1-KO	*P*	**6.05×10^{-4}**		0.0125	0.0500
RhAG-KO	*P*	0.136	0.456		0.0167
dKO	*P*	**0.00115**	0.847	0.0693	

Statistics Table 2 Comparison of SLC7A5 (LAT1) inferred abundance

Mouse		WT	AQP1-KO	RhAG-KO	dKO
	P \ α		α	α	α
WT			0.00833	0.0125	0.0100
AQP1-KO	*P*	0.143		0.0167	0.0500
RhAG-KO	*P*	0.426	0.496		0.0250
dKO	*P*	0.187	0.880	0.595	

Video Legends

Video 1. Video clip showing shapes of RBCs from a WT mouse

The video (1 frame per 5 sec) follows RBCs (collected and prepared as described in Methods[40], and used at an Hct of 2.5% to 3.0% as described in Methods[41]) of an RBC droplet as they fall freely through the plane of focus (40× objective, NA 1.35, with a 1.5× magnification selector), toward the surface of the coverslip. In the microvideo, the numerals that identify 18 specific RBCs are red when the cells are approximately in focus, but yellow either before they have fallen into focus or after they have fallen out of focus. This microvideo, which is typical of similar microvideos on a total of 3 mice, shows that the RBCs from WT mice are predominantly biconcave disks.

---

[40] See Methods>Preparation of RBCs>Collection of blood & ..>Processing of RBCs for assays 1–4

[41] See Methods>Still microphotography and microvideography of living RBCs

Video 2. Video clip showing shapes of RBCs from an *Aqp1*–/– (i.e., AQP1-KO) mouse

The video (1 frame per 5 sec) follows RBCs (collected and prepared as described in Methods[42], and used at an Hct of 2.5% to 3.0% as described in Methods[43]) of an RBC droplet as they fall freely through the plane of focus (40× objective, NA 1.35, with a 1.5× magnification selector), toward the surface of the coverslip. In the microvideo, the numerals that identify 14 specific RBCs are red when the cells are approximately in focus, but yellow either before they have fallen into focus or after they have fallen out of focus. This microvideo, which is typical of similar microvideos on a total of 3 mice, shows that the RBCs from AQP-KO mice are predominantly biconcave disks. Thus, one cannot attribute the observed 9% decrease in k_{HbO_2} value to a change in RBC shape.

[42] See Methods>Preparation of RBCs>Collection of blood & ..>Processing of RBCs for assays 1–4

[43] See Methods>Still microphotography and microvideography of living RBCs

Video 3. Video clip showing shapes of RBCs from an *Rhag*–/– (i.e., RhAG-KO) mouse

The video (1 frame per 5 sec) follows RBCs (collected and prepared as described in Methods[44], and used at an Hct of 2.5% to 3.0% as described in Methods[45]) of an RBC droplet as they fall freely through the plane of focus (40× objective, NA 1.35, with a 1.5× magnification selector), toward the surface of the coverslip. In the microvideo, the numerals that identify 13 specific RBCs are red when the cells are approximately in focus, but yellow either before they have fallen into focus or after they have fallen out of focus. This microvideo, which is typical of similar microvideos on a total of 3 mice, shows that the RBCs from Rhag–/ − mice are predominantly biconcave disks. Thus, one cannot attribute the observed 17% decrease in k_{HbO2} value to a change in RBC shape.

[44] See Methods>Preparation of RBCs>Collection of blood & ..>Processing of RBCs for assays 1–4

[45] See Methods>Still microphotography and microvideography of living RBCs

Video 4. Video clip showing shapes of RBCs from a *Aqp1*–/–*Rhag*–/– (i.e., dKO) mouse

The video (1 frame per 5 sec) follows RBCs (collected and prepared as described in Methods[46], and used at an Hct of 2.5% to 3.0% as described in Methods[47]) of an RBC droplet as they fall freely through the plane of focus (40× objective, NA 1.35, with a 1.5× magnification selector), toward the surface of the coverslip. In the microvideo, the numerals that identify 15 specific RBCs are red when the cells are approximately in focus, but yellow either before they have fallen into focus or after they have fallen out of focus. This microvideo, which is typical of similar microvideos on a total of 3 mice, shows that the RBCs from dKO mice are predominantly biconcave disks. Thus, one cannot attribute the observed 31% decrease in k_{HbO_2} value to a change in RBC shape.

[46] See Methods>Preparation of RBCs>Collection of blood & ..>Processing of RBCs for assays 1–4

[47] See Methods>Still microphotography and microvideography of living RBCs

References

Bedggood P, Ding Y & Metha A (2024). Changes to the shape, orientation and packing of red cells as a function of retinal capillary size. *Biomed Opt Express* **15,** 558–578.

Belkacemi A, Trost CF, Tinschert R, Flormann D, Malihpour M, Wagner C, Meyer MR, Beck A & Flockerzi V (2021). The TRPV2 channel mediates Ca^{2+} influx and the Δ9-THC-dependent decrease in osmotic fragility in red blood cells. *Haematologica* **106,** 2246–2250.

Benga G, Popescu O, Pop VI & Holmes RP (1986). p-(Chloromercuri)benzenesulfonate binding by membrane proteins and the inhibition of water transport in human erythrocytes. *Biochemistry* **25,** 1535–1538.

Bennett V (1983). Proteins involved in membrane--cytoskeleton association in human erythrocytes: spectrin, ankyrin, and band 3. *Meth Enzymol* **96,** 313–324.

Blank ME, Hoefner DM & Diedrich DF (1994). Morphology and volume alterations of human erythrocytes caused by the anion transporter inhibitors, DIDS and p-azidobenzylphlorizin. *Biochim Biophys Acta* **1192,** 223–233.

Boron WF (2010). Sharpey-Schafer lecture: gas channels. *Exp Physiol* **95,** 1107–1130.

Boron WF & Cooper GJ (1998). Effect of DIDS on the CO_2 permeability of the water channel AQP1. *FASEB J* **12,** 2174.

Bryk AH & Wiśniewski JR (2017). Quantitative Analysis of Human Red Blood Cell Proteome. *J Proteome Res* **16,** 2752–2761.

Cabantchik ZI & Rothstein A (1974*a*). Membrane proteins related to anion permeability of human red blood cells. I. Localization of disulfonic stilbene binding sites in proteins involved in permeation. *J Membr Biol* **15,** 207–226.

Cabantchik ZI & Rothstein A (1974*b*). Membrane proteins related to anion permeability of human red blood cells. II. Effects of proteolytic enzymes on disulfonic stilbene sites of surface proteins. *J Membr Biol* **15,** 227–248.

Capper MJ, Yang S, Stone AC, Vatansever S, Zilberg G, Mathiharan YK, Habib R, Hutchinson K, Zhao Y, Schlessinger A, Mezei M, Osman R, Zhang B & Wacker D (2023). Substrate binding and inhibition of the anion exchanger 1 transporter. *Nat Struct Mol Biol* **30,** 1495–1504.

Chen Y, Curran CP, Nebert DW, Patel KV, Williams MT & Vorhees CV (2012). Effect of vitamin C deficiency during postnatal development on adult behavior: functional phenotype of Gulo-/- knockout mice. *Genes Brain Behav* **11,** 269–277.

Chow PH, Cox CD, Pei JV, Anabaraonye N, Nourmohammadi S, Henderson SW, Martinac B, Abdulmalik O & Yool AJ (2021). Inhibition of the aquaporin-1 cation conductance by selected furan compounds reduces red blood cell sickling. *Front Pharmacol* **12,** 794791.

Coin JT & Olson JS (1979). The rate of oxygen uptake by human red blood cells. *J Biol Chem* **254,** 1178–1190.

Coste B, Mathur J, Schmidt M, Earley TJ, Ranade S, Petrus MJ, Dubin AE & Patapoutian A (2010). Piezo1 and Piezo2 are essential components of distinct mechanically activated cation channels. *Science* **330,** 55–60.

Cytek Biosciences (2024). Amnis® SpeedBead® Kit for ImageStream® Flow Cytometer. *Cytek Biosciences*. Available at: https://cytekbio.com/products/amnis-speedbead-kit-for-imagestream.

Donnan FG (1911). Theorie der Membrangleichgewichte und Membranpotentiale bei Vorhandensein von nicht dialysierenden Elektrolyten. Ein Beitrag zur physikalisch-chemischen Physiologie. *Zeitschrift für Elektrochemie und angewandte physikalische Chemie* **17,** 572–581.

Endeward V, Cartron J-P, Ripoche P & Gros G (2008). RhAG protein of the Rhesus complex is a CO_2 channel in the human red cell membrane. *FASEB J* **22,** 64–73.

Endeward V, Musa-Aziz R, Cooper GJ, Chen L-M, Pelletier MF, Virkki LV, Supuran CT, King LS, Boron WF & Gros G (2006). Evidence that aquaporin 1 is a major pathway for CO_2 transport across the human erythrocyte membrane. *FASEB J* **20,** 1974–1981.

Fang X-Z, Zhou T, Xu J-Q, Wang Y-X, Sun M-M, He Y-J, Pan S-W, Xiong W, Peng Z-K, Gao X-H & Shang Y (2021). Structure, kinetic properties and biological function of mechanosensitive Piezo channels. *Cell Biosci* **11,** 13.

Forstner H & Gnaiger E (1983). Appendix A. Calculation of equilibrium oxygen concentration. In *Polarographic oxygen sensors: aquatic and physiological applications*. Springer-Verlag, Berlin Heidelberg New York.

Gautier E-F, Leduc M, Cochet S, Bailly K, Lacombe C, Mohandas N, Guillonneau F, El Nemer W & Mayeux P (2018). Absolute proteome quantification of highly purified populations of circulating reticulocytes and mature erythrocytes. *Blood Adv* **2,** 2646–2657.

Genetet S, Desrames A, Chouali Y, Ripoche P, Lopez C & Mouro-Chanteloup I (2017). Stomatin modulates the activity of the Anion Exchanger 1 (AE1, SLC4A1). *Sci Rep* **7,** 46170.

Geyer RR, Musa-Aziz R & Boron WF (2011). Evidence that DIDS crosslinks Aquaporin 1 monomers. *FASEB J* **25,** 1039.26.

Geyer RR, Musa-Aziz R, Enkavi G, Mahinthichaichan P, Tajkhorshid E & Boron WF (2013). Movement of NH_3 through the human urea transporter B: a new gas channel. *Am J Physiol Renal Physiol* **304,** F1447-1457.

Gibbs JW (1878). On the equilibrium of heterogeneous substances. *Am J Sci & Arts* **16,** 441–458.

Gilson CR, Kraus TS, Hod EA, Hendrickson JE, Spitalnik SL, Hillyer CD, Shaz BH & Zimring JC (2009). A novel mouse model of red blood cell storage and posttransfusion in vivo survival. *Transfusion* **49,** 1546–1553.

Gnanasambandam R, Bae C, Gottlieb PA & Sachs F (2015). Ionic Selectivity and Permeation Properties of Human PIEZO1 Channels. *PLoS One* **10,** e0125503.

Golde WT, Gollobin P & Rodriguez LL (2005). A rapid, simple, and humane method for submandibular bleeding of mice using a lancet. *Lab Anim (NY)* **34,** 39–43.

Goodman SR, Kurdia A, Ammann L, Kakhniashvili D & Daescu O (2007). The human red blood cell proteome and interactome. *Exp Biol Med (Maywood)* **232,** 1391–1408.

Goossens D, Trinh-Trang-Tan M-M, Debbia M, Ripoche P, Vilela-Lamego C, Louache F, Vainchenker W, Colin Y & Cartron J-P (2010). Generation and characterisation of Rhd and Rhag null mice. *Br J Haematol* **148,** 161–172.

Groves JD & Tanner MJ (1992). Glycophorin A facilitates the expression of human band 3-mediated anion transport in *Xenopus* oocytes. *J Biol Chem* **267,** 22163–22170.

Groves JD & Tanner MJ (1994). The effects of glycophorin A on the expression of the human red cell anion transporter (band 3) in *Xenopus* oocytes. *J Membr Biol* **140,** 81–88.

Gruswitz F, Chaudhary S, Ho JD, Schlessinger A, Pezeshki B, Ho C-M, Sali A, Westhoff CM & Stroud RM (2010). Function of human Rh based on structure of RhCG at 2.1 Å. *Proc Natl Acad Sci USA* **107,** 9638–9643.

Habibabady ZA, Sendil S, Ellett F, Pollok F, Elias GF, French BM, Sun W, Braileanu G, Burdorf L, Irimia D, Pierson RN & Azimzadeh AM (2022). Human erythrocyte fragmentation during ex-vivo pig organ perfusion. *Xenotransplantation* **29,** e12729.

Hamasaki N (1999). The role of band 3 protein in oxygen delivery by red blood cells. *Indian J Clin Biochem* **14,** 49–58.

Hamilton NB, Attwell D & Hall CN (2010). Pericyte-mediated regulation of capillary diameter: a component of neurovascular coupling in health and disease. *Front Neuroenergetics* **2,** 5.

Hoefner DM, Blank ME, Davis BM & Diedrich DF (1994). Band 3 antagonists, p-azidobenzylphlorizin and DIDS, mediate erythrocyte shape and flexibility changes as characterized by digital image morphometry and microfiltration. *J Membr Biol* **141,** 91–100.

Holm S (1979). A simple sequentially rejective multiple test procedure. *Scandinavian Journal of Statistics* **6,** 65–70.

Hsu K, Lee T-Y, Lin J-Y & Chen P-L (2022). A balance between transmembrane-mediated ER/Golgi retention and forward trafficking signals in glycophorin-anion exchanger-1 interaction. *Cells* **11,** 3512.

Hsu L & Morrison M (1983). The interaction of human erythrocyte Band 3 with cytoskeletal components. *Arch Biochem Biophys* **227,** 31–38.

Huynh KW, Jiang J, Abuladze N, Tsirulnikov K, Kao L, Shao X, Newman D, Azimov R, Pushkin A, Zhou ZH & Kurtz I (2018). CryoEM structure of the human SLC4A4 sodium-coupled acid-base transporter NBCe1. *Nat Commun* **9,** 900.

Jauréguiberry S et al. (2014). Postartesunate delayed hemolysis is a predictable event related to the lifesaving effect of artemisinins. *Blood* **124,** 167–175.

Kakhniashvili DG, Bulla LA & Goodman SR (2004). The human erythrocyte proteome: analysis by ion trap mass spectrometry. *Mol Cell Proteomics* **3,** 501–509.

Kalfa T & McGrath KE (2018). Analysis of erythropoiesis using imaging flow cytometry. *Methods Mol Biol* **1698,** 175–192.

Karamatic Crew V et al. (2023). Missense mutations in PIEZO1, which encodes the Piezo1 mechanosensor protein, define Er red blood cell antigens. *Blood* **141,** 135–146.

Kim J, Gómez-Pastora J, Weigand M, Potgieter M, A Walters N, Reátegui E, F Palmer A, Yazer M, Zborowski M & Chalmers JJ (2019). A subpopulation of monocytes in normal human blood has significant magnetic susceptibility: Quantification and potential implications. *Cytometry A* **95,** 478–487.

Kreuzer F (1982). Oxygen supply to tissues: the Krogh model and its assumptions. *Experientia* **38,** 1415–1426.

Krogh A (1919). The number and distribution of capillaries in muscles with calculations of the oxygen pressure head necessary for supplying the tissue. *J Physiol (Lond)* **52,** 409–415.

Kuchel PW, Coy A & Stilbs P (1997). NMR "diffusion-diffraction" of water revealing alignment of erythrocytes in a magnetic field and their dimensions and membrane transport characteristics. *Magn Reson Med* **37,** 637–643.

Lambrecht BN, Vanderkerken M & Hammad H (2018). The emerging role of ADAM metalloproteinases in immunity. *Nat Rev Immunol* **18,** 745–758.

Lee YQ, Goh ASP, Ch'ng JH, Nosten FH, Preiser PR, Pervaiz S, Yadav SK & Tan KSW (2014). A high-content phenotypic screen reveals the disruptive potency of quinacrine and 3',4'-dichlorobenzamil on the digestive vacuole of Plasmodium falciparum. *Antimicrob Agents Chemother* **58,** 550–558.

Loken MR, Parks DR & Herzenberg LA (1977). Identification of cell asymmetry and orientation by light scattering. *J Histochem Cytochem* **25,** 790–795.

Majetschak M & Sorell LT (2008). Immunological methods to quantify and characterize proteasome complexes: development and application. *J Immunol Methods* **334,** 91–103.

Mankelow TJ, Satchwell TJ & Burton NM (2012). Refined views of multi-protein complexes in the erythrocyte membrane. *Blood Cells Mol Dis* **49,** 1–10.

Mantel P-Y, Hoang AN, Goldowitz I, Potashnikova D, Hamza B, Vorobjev I, Ghiran I, Toner M, Irimia D, Ivanov AR, Barteneva N & Marti M (2013). Malaria-infected erythrocyte-derived microvesicles mediate cellular communication within the parasite population and with the host immune system. *Cell Host Microbe* **13,** 521–534.

Marfatia SM, Lue RA, Branton D & Chishti AH (1994). In vitro binding studies suggest a membrane-associated complex between erythroid p55, protein 4.1, and glycophorin C. *J Biol Chem* **269,** 8631–8634.

Marin M, Peltier S, Hadjou Y, Georgeault S, Dussiot M, Roussel C, Hermine O, Roingeard P, Buffet PA & Amireault P (2022). Storage-induced micro-erythrocytes can be quantified and sorted by flow cytometry. *Front Physiol* **13,** 838138.

Mathai JC, Mori S, Smith BL, Preston GM, Mohandas N, Collins M, van Zijl PC, Zeidel ML & Agre P (1996). Functional analysis of aquaporin-1 deficient red cells. The Colton-null phenotype. *J Biol Chem* **271,** 1309–1313.

McGrath KE, Catherman SC & Palis J (2017). Delineating stages of erythropoiesis using imaging flow cytometry. *Methods* **112,** 68–74.

Missner A & Pohl P (2009). 110 years of the Meyer-Overton rule: predicting membrane permeability of gases and other small compounds. *Chemphyschem* **10,** 1405–1414.

Mosior M, Białas WA, Wróbel A & Gomułkiewicz J (1992). Critical cell volume and shape of bovine erythrocytes. *Gen Physiol Biophys* **11,** 499–506.

Muravyov A & Tikhomirova I (2012). Role Ca^{2+} in mechanisms of the red blood cells microrheological changes. *Adv Exp Med Biol* **740,** 1017–1038.

Musa-Aziz R, Chen L & Boron WF (2007*a*). The CO_2/NH_3 Selectivity of AQP1, AQP4, and AQP5 and How It is Affected by DIDS. *J Am Soc Nephrol* **18,** P6A.

Musa-Aziz R, Chen L-M & Boron WF (2007*b*). Differential effects of DIDS on the CO_2 vs NH_3 permeability of AQP1, AmtB, and RhAG. *Proceedings of the International Congress of Nephrology, Rio de Janeiro, Brazil*.

Musa-Aziz R, Geyer RR & Boron WF (2025). Mechanism of CO_2 and NH_3 transport through human aquaporin 1: Evidence for parallel CO_2 pathways. *bioRxiv*; DOI: https://doi.org/10.1101/2025.02.28.640247.

Neelam S, Kakhniashvili DG, Wilkens S, Levene SD & Goodman SR (2011). Functional 20S proteasomes in mature human red blood cells. *Exp Biol Med (Maywood)* **236,** 580–591.

Nicolas V, Le Van Kim C, Gane P, Birkenmeier C, Cartron J-P, Colin Y & Mouro-Chanteloup I (2003). Rh-RhAG/ankyrin-R, a new interaction site between the membrane bilayer and the red cell skeleton, is impaired by Rh(null)-associated mutation. *J Biol Chem* **278,** 25526–25533.

Notariale R, Längst E, Perrone P, Crettaz D, Prudent M & Manna C (2022). Effect of mercury on membrane proteins, anionic transport and cell morphology in human erythrocytes. *Cell Physiol Biochem* **56,** 500–513.

Nunomura W, Sasakura D, Shiba K, Nakamura S, Kidokoro S-I & Takakuwa Y (2011). Structural stabilization of protein 4.1R FERM domain upon binding to apo-calmodulin: novel insights into the biological significance of the calcium-independent binding of calmodulin to protein 4.1R. *Biochem J* **440,** 367–374.

Nunomura W & Takakuwa Y (2006). Regulation of protein 4.1R interactions with membrane proteins by Ca^{2+} and calmodulin. *Front Biosci* **11,** 1522–1539.

Nurden A (2021). Profiling the genetic and molecular characteristics of glanzmann thrombasthenia: can it guide current and future therapies? *J Blood Med* **12,** 581–599.

Nurden AT, Fiore M, Nurden P & Pillois X (2011). Glanzmann thrombasthenia: a review of ITGA2B and ITGB3 defects with emphasis on variants, phenotypic variability, and mouse models. *Blood* **118,** 5996–6005.

Occhipinti R, Zhao P, Huffman DE, Moss FJ & Boron WF (2025). Role of channels in the O_2 permeability of murine red blood cells. III. Mathematical modeling and simulations. *J Physiol*.

O'Connell KE, Mikkola AM, Stepanek AM, Vernet A, Hall CD, Sun CC, Yildirim E, Staropoli JF, Lee JT & Brown DE (2015). Practical murine hematopathology: A comparative review and implications for research. *Comp Med* **65,** 96–113.

Pang AJ & Reithmeier RAF (2009). Interaction of anion exchanger 1 and glycophorin A in human erythroleukaemic K562 cells. *Biochem J* **421,** 345–356.

Pasini EM, Kirkegaard M, Mortensen P, Lutz HU, Thomas AW & Mann M (2006). In-depth analysis of the membrane and cytosolic proteome of red blood cells. *Blood* **108,** 791–801.

Pasini EM, Kirkegaard M, Salerno D, Mortensen P, Mann M & Thomas AW (2008). Deep coverage mouse red blood cell proteome: a first comparison with the human red blood cell. *Mol Cell Proteomics* **7,** 1317–1330.

Pesciotta EN, Sriswasdi S, Tang H-Y, Mason PJ, Bessler M & Speicher DW (2012). A label-free proteome analysis strategy for identifying quantitative changes in erythrocyte membranes induced by red cell disorders. *J Proteomics*; DOI: 10.1016/j.jprot.2012.08.010.

Pinto RN, Sebastian JA, Parsons MJ, Chang TC, Turner TR, Acker JP & Kolios MC (2019). Label-free analysis of red blood cell storage lesions using imaging flow cytometry. *Cytometry A* **95,** 976–984.

Pruessmeyer J, Hess FM, Alert H, Groth E, Pasqualon T, Schwarz N, Nyamoya S, Kollert J, van der Vorst E, Donners M, Martin C, Uhlig S, Saftig P, Dreymueller D & Ludwig A (2014). Leukocytes require ADAM10 but not ADAM17 for their migration and inflammatory recruitment into the alveolar space. *Blood* **123,** 4077–4088.

Reid ME, Chasis JA & Mohandas N (1987). Identification of a functional role for human erythrocyte sialoglycoproteins beta and gamma. *Blood* **69,** 1068–1072.

Reid ME, Takakuwa Y, Conboy J, Tchernia G & Mohandas N (1990). Glycophorin C content of human erythrocyte membrane is regulated by protein 4.1. *Blood* **75,** 2229–2234.

Roudier N, Verbavatz JM, Maurel C, Ripoche P & Tacnet F (1998). Evidence for the presence of aquaporin-3 in human red blood cells. *J Biol Chem* **273,** 8407–8412.

Rungaldier S, Oberwagner W, Salzer U, Csaszar E & Prohaska R (2013). Stomatin interacts with GLUT1/SLC2A1, band 3/SLC4A1, and aquaporin-1 in human erythrocyte membrane domains. *Biochim Biophys Acta* **1828,** 956–966.

Russell ES, Neufeld EF & Higgins CT (1951). Comparison of normal blood picture of young adults from 18 inbred strains of mice. *Proc Soc Exp Biol Med* **78,** 761–766.

Ryu M-S, Lichten LA, Liuzzi JP & Cousins RJ (2008). Zinc transporters ZnT1 (Slc30a1), Zip8 (Slc39a8), and Zip10 (Slc39a10) in mouse red blood cells are differentially regulated during erythroid development and by dietary zinc deficiency. *J Nutr* **138,** 2076–2083.

Safeukui I, Buffet PA, Deplaine G, Perrot S, Brousse V, Ndour A, Nguyen M, Mercereau-Puijalon O, David PH, Milon G & Mohandas N (2012). Quantitative assessment of sensing and sequestration of spherocytic erythrocytes by the human spleen. *Blood* **120,** 424–430.

Safeukui I, Buffet PA, Perrot S, Sauvanet A, Aussilhou B, Dokmak S, Couvelard A, Hatem DC, Mohandas N, David PH, Mercereau-Puijalon O & Milon G (2013). Surface area loss and increased sphericity account for the splenic entrapment of subpopulations of Plasmodium falciparum ring-infected erythrocytes. *PLoS ONE* **8,** e60150.

Salomao M, Zhang X, Yang Y, Lee S, Hartwig JH, Chasis JA, Mohandas N & An X (2008). Protein 4.1R-dependent multiprotein complex: new insights into the structural organization of the red blood cell membrane. *Proc Natl Acad Sci U S A* **105,** 8026–8031.

Schlatzer DM, Dazard J-E, Dharsee M, Ewing RM, Ilchenko S, Stewart I, Christ G & Chance MR (2009). Urinary protein profiles in a rat model for diabetic complications. *Mol Cell Proteomics* **8,** 2145–2158.

Secomb TW (2017). Blood Flow in the Microcirculation. *Annual Review of Fluid Mechanics* **49,** 443–461.

Stachon A, Sondermann N, Imohl M & Krieg M (2002). Nucleated red blood cells indicate high risk of in-hospital mortality. *J Lab Clin Med* **140,** 407–412.

Sugie J, Intaglietta M & Sung LA (2018). Water transport and homeostasis as a major function of erythrocytes. *Am J Physiol Heart Circ Physiol*; DOI: 10.1152/ajpheart.00263.2017.

Suzuki J, Imanishi E & Nagata S (2014). Exposure of phosphatidylserine by Xk-related protein family members during apoptosis. *J Biol Chem* **289,** 30257–30267.

Takakuwa Y & Mohandas N (1988). Modulation of erythrocyte membrane material properties by Ca^{2+} and calmodulin. Implications for their role in regulation of skeletal protein interactions. *J Clin Invest* **82,** 394–400.

Tzounakas VL, Dzieciatkowska M, Anastasiadi AT, Karadimas DG, Vergaki A, Siourounis P, Stamoulis K, Papassideri IS, Kriebardis AG, D'Alessandro A & Antonelou MH (2022). Red cell proteasome modulation by storage, redox metabolism and transfusion. *Blood Transfus* **20,** 27–39.

Vaisey G, Banerjee P, North AJ, Haselwandter CA & MacKinnon R (2022). Piezo1 as a force-through-membrane sensor in red blood cells. *Elife* **11,** e82621.

Vallese F, Kim K, Yen LY, Johnston JD, Noble AJ, Calì T & Clarke OB (2022). Architecture of the human erythrocyte ankyrin-1 complex. *Nat Struct Mol Biol* **29,** 706–718.

Van Dort HM, Knowles DW, Chasis JA, Lee G, Mohandas N & Low PS (2001). Analysis of integral membrane protein contributions to the deformability and stability of the human erythrocyte membrane. *J Biol Chem* **276,** 46968–46974.

Vitry M-A, Hanot Mambres D, Deghelt M, Hack K, Machelart A, Lhomme F, Vanderwinden J-M, Vermeersch M, De Trez C, Pérez-Morga D, Letesson J-J & Muraille E (2014). Brucella melitensis invades murine erythrocytes during infection. *Infect Immun* **82,** 3927–3938.

Webb KL, Dominelli PB, Baker SE, Klassen SA, Joyner MJ, Senefeld JW & Wiggins CC (2021). Influence of high hemoglobin-oxygen affinity on humans during hypoxia. *Front Physiol* **12,** 763933.

Welch BL (1947). The generalization of 'Student's' problem when several different population variances are involved. *Biometrika* **34,** 28–35.

Westen EA & Prange HD (2003). A reexamination of the mechanisms underlying the arteriovenous chloride shift. *Physiol Biochem Zool* **76,** 603–614.

Wiśniewski JR (2017). Filter-aided sample preparation: The versatile and efficient method for proteomic analysis. *Meth Enzymol* **585,** 15–27.

Wong P (1994). Mechanism of control of erythrocyte shape: a possible relationship to band 3. *J Theor Biol* **171,** 197–205.

Wong P (2004). A basis of the acanthocytosis in inherited and acquired disorders. *Med Hypotheses* **62,** 966–969.

Wong P (2018). An explanation of the reversal of erythrocyte echinocytosis by incubation and storage by serum albumin. *Clin Hemorheol Microcirc* **68,** 383–389.

Yabas M, Coupland LA, Cromer D, Winterberg M, Teoh NC, D'Rozario J, Kirk K, Bröer S, Parish CR & Enders A (2014). Mice deficient in the putative phospholipid flippase ATP11C exhibit altered erythrocyte shape, anemia, and reduced erythrocyte life span. *J Biol Chem* **289,** 19531–19537.

Yang B, Ma T & Verkman AS (2001). Erythrocyte water permeability and renal function in double knockout mice lacking aquaporin-1 and aquaporin-3. *J Biol Chem* **276,** 624–628.

Yang B & Verkman AS (2002). Analysis of double knockout mice lacking aquaporin-1 and urea transporter UT-B. Evidence for UT-B-facilitated water transport in erythrocytes. *J Biol Chem* **277,** 36782–36786.

You X, Ryu M-J, Cho E, Sang Y, Damnernsawad A, Zhou Y, Liu Y, Zhang J & Lee Y (2021). Embryonic expression of NrasG 12 D leads to embryonic lethality and cardiac defects. *Front Cell Dev Biol* **9,** 633661.

Zhao P, Geyer RR & Boron WF (2017). A novel stopped-flow assay for quantitating carbonic-anhydrase activity and assessing red-blood-cell hemolysis. *Front Physiol* **8,** 169.

Zhao P, Moss FJ, Occhipinti R, Geyer RR, Huffman DE, Gros G & Boron W F (2025). Role of channels in the O_2 permeability of murine red blood cells. I. Stopped-flow and hematological studies. *J Physiol*.

Zhekova HR, Jiang J, Wang W, Tsirulnikov K, Kayık G, Khan HM, Azimov R, Abuladze N, Kao L, Newman D, Noskov SY, Tieleman DP, Hong Zhou Z, Pushkin A & Kurtz I (2022). CryoEM structures of anion exchanger 1 capture multiple states of inward- and outward-facing conformations. *Commun Biol* **5,** 1372.

Zheng X, Zhang C, Cao H, Zhou X, Liu Z & Wang J (2023). Zinc cations uniquely stabilize cell membrane for cell cryopreservation. *Nano Lett* **23,** 9920–9927.

Zingoni A, Vulpis E, Loconte L & Santoni A (2020). NKG2D Ligand Shedding in Response to Stress: Role of ADAM10. *Front Immunol* **11,** 447.

Additional Information

Data availability statement

The data that support the findings of this study are available from the corresponding author. W.F.B., upon reasonable request.

Competing interests

The authors declare that they have no competing interests.

Author contributions

F.J.M., P.Z., & W.F.B. designed the study; F.J.M. performed mass spectrometry; F.J.M also performed the flow cytometry experiments and analyzed the data together with J.W.J.; P.Z., A.I.S. & S.T. performed the microvideography of tumbling blood cells and analyzed the data with D.E.H who assisted in capturing still images from videos; A.B.W. produced ghosts for mass spectrometry; P.Z. made blood smears and H.J.M. performed the analysis; F.J.M., P.Z., R.O. & W.F.B. wrote the manuscript.

Supporting Information

Supporting file 1: SI_2--MassSpecData.xlsx

Supporting file 2: SI_2--Suppl_Tables_MassSpec_Statistics_For Fig10 & Table7.xlsx

Supporting video 1: xSupp_Video_1--WT.wmv

Supporting video 2: xSupp_Video_2--AQP1-KO.wmv

Supporting video 3: xSupp_Video_3--RhAG-KO.wmv

Supporting video 4: xSupp_Video_4--dKO.wmv